City, University of London Institutional Repository

Dynamics of Post-Injection Fuel Flow in Mini-Sac Diesel Injectors Part 1: Admission of External Gases and Implications for Deposit Formation

Kassandra Makri, Russel Lockett[#*], Mahesh Jeshani

Department of Mechanical Engineering & Aeronautics, City, University of London,

Northampton Square, London, EC1V 0HB, United Kingdom

[#]Now at Exa-flo Ltd, 18 Pennine Rise, Flitwick, Bedford, MK45 1TP, UK

[*]Corresponding author: r.d.lockett@city.ac.uk

Abstract

Samples of unadditized, middle distillate diesel fuel were injected through real-size optically accessible mini-sac diesel injectors into ambient air at common rail pressures of 250 bar and 350 bar respectively. High-resolution images of white light scattered from the internal mini-sac and nozzle flow were captured on a high-speed monochrome video camera. Following the end of each injection, the momentum-driven evacuation of fuel liquid from the mini-sac and nozzle holes resulted in the formation of a vapour cloud and bubbles in the mini-sac, and vapour capsules in the nozzle holes. This permitted external gas to gain entrance to the nozzle holes.

The diesel fuel in the mini-sac was observed to rotate with large initial vorticity, which decayed until the fuel became stationary. The diesel fuel remaining in the nozzle holes was observed to move inwards towards the mini-sac or outwards towards the nozzle exit in concert with the rotational flow in the mini-sac. The mini-sac bubbles' internal pressure differences revealed that the bubbles must have contained previously dissolved oxygen and nitrogen. Under diesel engine operating conditions, this multi-phase mixture would be highly reactive and could initiate local pyrolysis and/or oxidation reactions. Finally, the dynamical behaviour of the diesel fuel in the nozzle holes would support the admission of external hot combustion gases into the nozzle holes, establishing the conditions for oxidation/pyrolysis reactions with surrounding liquid fuel films.

Keywords: Diesel, fuel injection system, internal flow, mini-sac, soot, deposit, scattering, cavitation.

1. Introduction

Most modern passenger car and truck diesel engines operate using high pressure common rail diesel fuel injection equipment (FIE), which are comprised of a high pressure fuel pump supplying diesel to the fuel injectors via a common high pressure fuel accumulator (termed the common rail) [1, 2]. Conventionally, the injectors supply the diesel fuel to the engine cylinders through multi-hole nozzles, which are exposed to the high pressure fuel through the actuation of a nozzle needle. This actuation may be direct, through the deployment of a piezo-electric stack [3 – 5]. Alternatively, the actuation may be indirect, by using the force difference achieved at the bottom of the needle relative to the top via an internal pressure management system that is actuated via a magnetic solenoid acting on a ferromagnetic steel push rod [1, 2, 6, 7]. In order to comply with international regulations requiring reduced exhaust-out emissions, FIE manufacturers have developed injectors that are able to support multiple injections involving repeatedly accurate injected fuel mass. The sprays emitted from these injectors are required to atomise effectively in the piston bowl in order to entrain and utilise all the available air effectively. These requirements have resulted in the development of six-, nine- and twelve-hole high efficiency diesel nozzles with small, conical holes and profiled nozzle inlets [8, 9], supported by accumulator pressures of up to 3,000 bar [10 – 12].

The development and deployment of high efficiency nozzles in commercial FIE has resulted in increased injector deposits [13 – 15], which has, in turn, resulted in inconsistent and/or reduced engine performance, increased engine-out emissions, and in extreme circumstances, injector failure (needle stick, blocked holes) [16]. Previously, injector nozzles with cylindrical holes produced significant geometric cavitation, which supported the removal of early deposition. However, the cavitation occurring in the nozzle holes during injection also reduced the available flow area and nozzle discharge coefficient [17, 18]. Deposits that are observed to form inside the injector nozzle and on the injector needle during operation have been the subject of a significant body of research over the last ten years [15, 16, 19 – 29]. The detail of the mechanisms involved in internal deposit formation are not well understood, and a considerable amount of research is required to resolve this difficult problem. Deposits located in the nozzle holes, mini-sac and on the base of the injector needle are most likely formed

through an interaction between external combustion gases and components of the diesel fuel [28]. Deposits formed on the pushrod needle, armature, and other related components upstream of the injector needle are most likely to originate from components transported in the fuel [25]. A variety of internal injector deposits have been identified to form inside modern diesel injectors. These are: (1) waxy, soapy deposits observed to form on the needle and armature, which can lead to injector failure through needle stick, (2) organic amide polymeric deposits that form a hardened lacquer on internal surfaces, (3) sticky brown/black tar deposits associated with aged fuels, and (4) layered, hard, crusty, black, carbonaceous deposits with a mixture of crystallised carbon graphite, condensed aliphatic and poly-cyclic aromatic hydrocarbons (PAHs) located in injector nozzle holes and injector nozzle tips [25, 26].

Metals such as Zinc (Zn) are employed as active ingredients in lubricant oils, which were used in the past in lubricity additives in diesel. Unfortunately, Zinc is indicated in accelerated internal deposition in the form of insoluble zinc salts, and is consequently employed in the CEC F-98-08 injector nozzle coking test [27, 28]. Other metals such as Sodium (Na), Calcium (Ca), Potassium (K) and Phosphorous (Ph) are often present in the fuel through exposure to sea water during transportation, or their inclusion in corrosion inhibitors, anti-oxidants, de-icing agents, and salt dryers [22, 25]. Iron (Fe) and Chromium (Cr) particles originating from hydro-erosion of the hardened steel comprising the components in the diesel fuel injection system are deposited in the diesel fuel as it makes its way through the high-pressure fuel injection system [29, 30]. These metals are able to react with acids present in additized diesel fuel to form insoluble salt deposits [25]. Acids are ubiquitous in modern commercial diesel fuels, in the form of various carboxylic acids (formed through fuel ageing/pyrolysis/oxidation), and in a variety of diesel fuel additives (forming key components in lubricity and flow improvers, corrosion inhibitors, detergents, surfactants, anti-oxidants etc) [25]. Examples include: (1) alkyl and alkenyl succinic acids used as corrosion inhibitors, (2) mono- and di-fatty acids used as lubricity improvers, and (3) polyisobutylene succinimides (PIBSIs) used as deposit control additives (DCAs). Metal ions reacting with acids leads to the formation of insoluble salts which deposit inside small-clearance injector surfaces in the form of waxy soaps. Mono- and di- fatty acids are able to react with polyisobutylene succinimides (PIBSIs) to form brown, sticky organic amides and hard, peptide polymer lacquer deposits

[25, 26]. Stressed and aged diesel fuels can be degraded to produce black, crusty, carbonaceous deposits that are found in fuel tanks, fuel filters, injector nozzle holes and on injector tips. These types of deposits have been found to contain amorphous carbon, crystalline graphitic carbon, and aliphatic and poly-cyclic aromatic hydrocarbon (PAH) condensates [25, 26].

Fuel metering at the high pressure pump and injector needle control results in a significant fraction of high-pressure fuel being returned back to the fuel tank via control valves. This implies that a significant fraction of the diesel fuel has been recirculated through the high-pressure pump, pressure accumulator and/or injectors, prior to admission to the engine. The recirculation of high-pressure fuel across control valve nozzles is capable of stressing the fuel, which may lead to premature ageing and degradation [30 – 35]. Four types of deposits have been observed to form throughout the fuel injection system in these studies. They are (1) a hard lacquer coating the internal stainless steel surfaces, (2) sticky brown/black deposits (likely to be caused by fuel ageing and degradation), (3) crusty brown/black carbonaceous aggregates that collect in small clearance regions, and (4) black particles and aggregates with a ferromagnetic response [30, 32]. It is believed that the particles and aggregates with ferromagnetic properties originate from iron particles formed through hydrodynamic erosion of the internal steel surfaces, which then form a substrate for surface reactions, condensation and other deposition [30].

Consequently, fuel-derived deposits and sediments have been observed to develop at the entrance to and inside the nozzle holes in mini-sac multihole diesel injectors [25, 26]. High pressure fuel injection equipment employing injectors with small diameter nozzle holes interact with the engine block and the combustion gases formed during combustion in the engine, resulting in injector body temperatures ranging between 500 K and 600 K during normal engine operation. The injector body, mini-sac and small nozzle holes expose the fuel remaining in the injector between injections to large temperatures that are able to initiate and support oxidation and pyrolysis. This effect is known to exacerbate the rate and amount of carbonaceous deposit formation occurring in the nozzle holes and nozzle tip, thereby contributing to fouling problems by accelerating the ageing of the fuel.

This paper suggests a potential mechanism for deposit formation in mini-sac injector nozzle holes and mini-sac walls. Following the end of the injection event, bubbles and/or vapour capsules were observed to form in the nozzle holes, moving in concert with the circumferential flow occurring in the mini-sac. The local motion of the bubbles observed in the nozzle passages and the mini-sac reflects the local motion of the bulk fluid. Significant inwards motion of the diesel fuel retained in the nozzle holes between injections that permit the admission of external gases into the nozzle holes has been observed. In engine operating conditions, this may support the formation of carbonaceous deposits inside the nozzle through surface oxidation and oxygen assisted pyrolysis.

2. Experimental

2.1 Fuel Injection System

The high-pressure common rail diesel fuel injection system shown in Figure 1 was manufactured at City, University of London, and was capable of generating an accumulator pressure of up to 1,500 bar, and a precise quantity of fuel through the injector at a user-determined rate. The fuel was delivered from the tank to the high pressure pump via a rotary vane pump and a 5μm polypropylene filter. The high-pressure fuel leaving the diesel pump was discharged to the pressure accumulator, which in turn, was connected to an optically accessible mini-sac diesel injector via a fast response Kulite ETMER-1-375M-3500BARSG pressure transducer, that was rated to 3,500 bar sealed gauge with a sensitivity and zero offset of 1.189mV/bar and 500mV ± 50mV respectively.

The control of the injection process was achieved by a customized timing control box which sent a TTL pulse train to the injector driver. This was linked to a fixed pump shaft phase angle, ensuring a repeatable delivery pressure for each injection. The injector driver activated a magnetic solenoid inside the injector body, which activated the injector push rod. The internal fuel pressure control system supported the lift and return of the injector needle, enabling the fuel flow through the mini-sac and nozzle holes into the surrounding air.
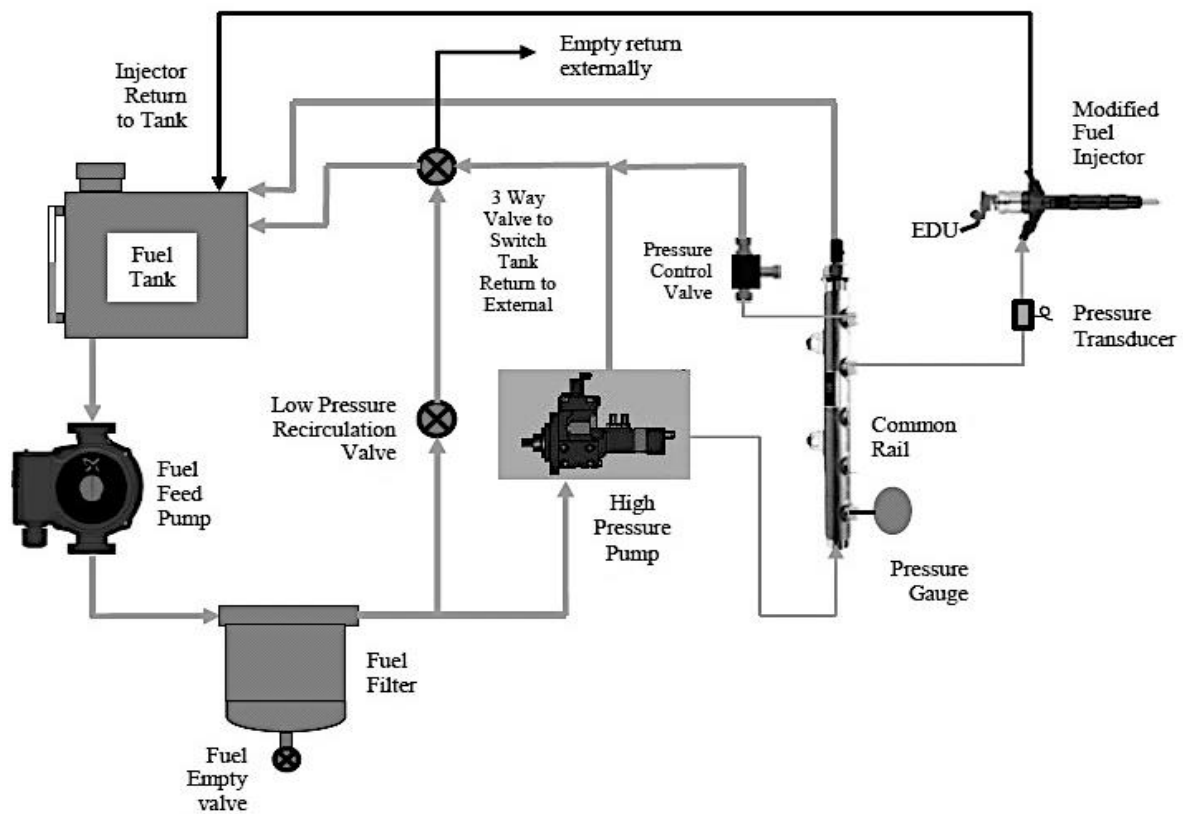
Figure 1: Schematic of the customised fuel injection system.

A 3.1 Hz TTL pulse train of 4.0 ms duration was provided to the injector driver. The consequent needle lift rate was measured to be approximately 0.12 mm/ms for 3.0 ms, followed by a maximum lift period of 0.3 ms, followed by a 1.6 ms period of needle return. Hence the needle returned to its initial position approximately 5.5 ms – 6.0 ms after the electronic start-of-injection (SoI) signal. The needle lift profile was measured optically [36], and by using a magnetic induction sensor imbedded in a VCO injector of similar design [37]. The lift profiles corresponding to 350 bar accumulator pressure are shown in Figure 2. These are typical for engines operating at idle or low speed and load.

The accumulator pressure was measured using a pressure gauge attached to one of the outlet ports on the common rail. An adjustable pressure control valve was employed to control the common rail fuel pressure, based on the reading obtained from the pressure gauge. The temperature in the fuel delivery system was measured at the inlet of the high pressure pump, using a K-type thermocouple. This was

also connected to a chilled water cooling system which was employed to maintain the fuel temperature in the fuel injection system at a predetermined set value of 40 ℃.
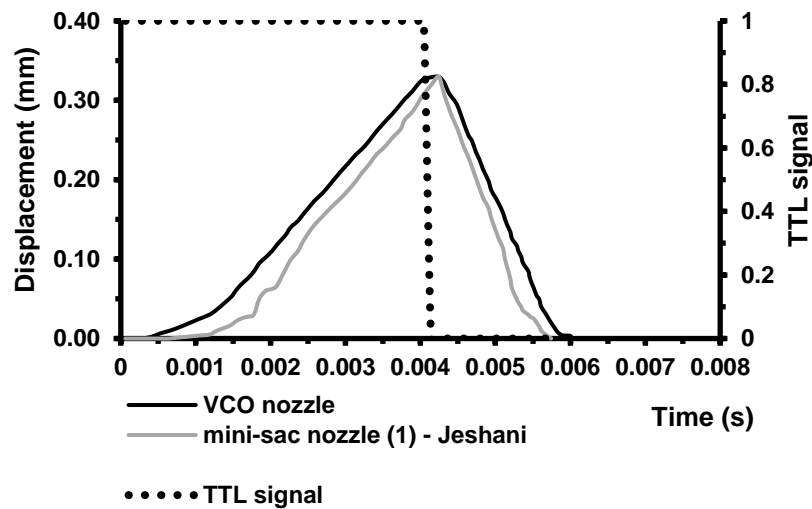

Figure 2: Needle lift profile as a function of time relative to the injection TTL pulse. (1) The black line needle lift profile was measured using a VCO injector with an induction sensor [36]. (2) The grey line needle lift profile was measured optically using successive image frames [37].

2.2 Optical Nozzle Design

A modified commercial six-hole mini-sac diesel injector nozzle was employed in these experiments. Figure 3 (a) shows a conceptual image of a mini-sac diesel injector nozzle, with the needle producing a sealed surface against the sides of the nozzle body, located below the mini-sac, which in turn, provides the access to the nozzle holes. Figures 3 (b) and (c) show the side view and an inclined view of the 6-hole commercial nozzle employed in this investigation. Figure 3 (d) shows an inclined view of a similar mini-sac nozzle that has been processed in order to locate an optically accessible nozzle tip. The base of the processed mini-sac nozzle was machined to remove the mini-sac tip, introducing a recessed annulus with polished flat surface to hold and seal the replica acrylic nozzle tip, which provided optical access to the mini-sac and nozzle holes. Figures 3 (e) and (f) show an inclined view and side view of an acrylic nozzle tip located on the processed, recessed annulus of the injector nozzle. The acrylic tips were machined at City, University of London, retaining the mini-sac geometry and the location of the six nozzle hole entrances. However, the requirement to maintain optical access to all of the nozzle holes necessitated an adjustment of the 15° nozzle hole angle in the original injector to 25° in the optically accessible acrylic tip. Figure 4 (a) shows the design schematic used to manufacture the acrylic nozzle

tips. However, only two of the nozzle holes could be viewed in detail due to the very small depth of field achievable during imaging; thus these two holes were designed to be manufactured on opposite faces, and are marked as holes 1 and 2 in Figure 4 (b).
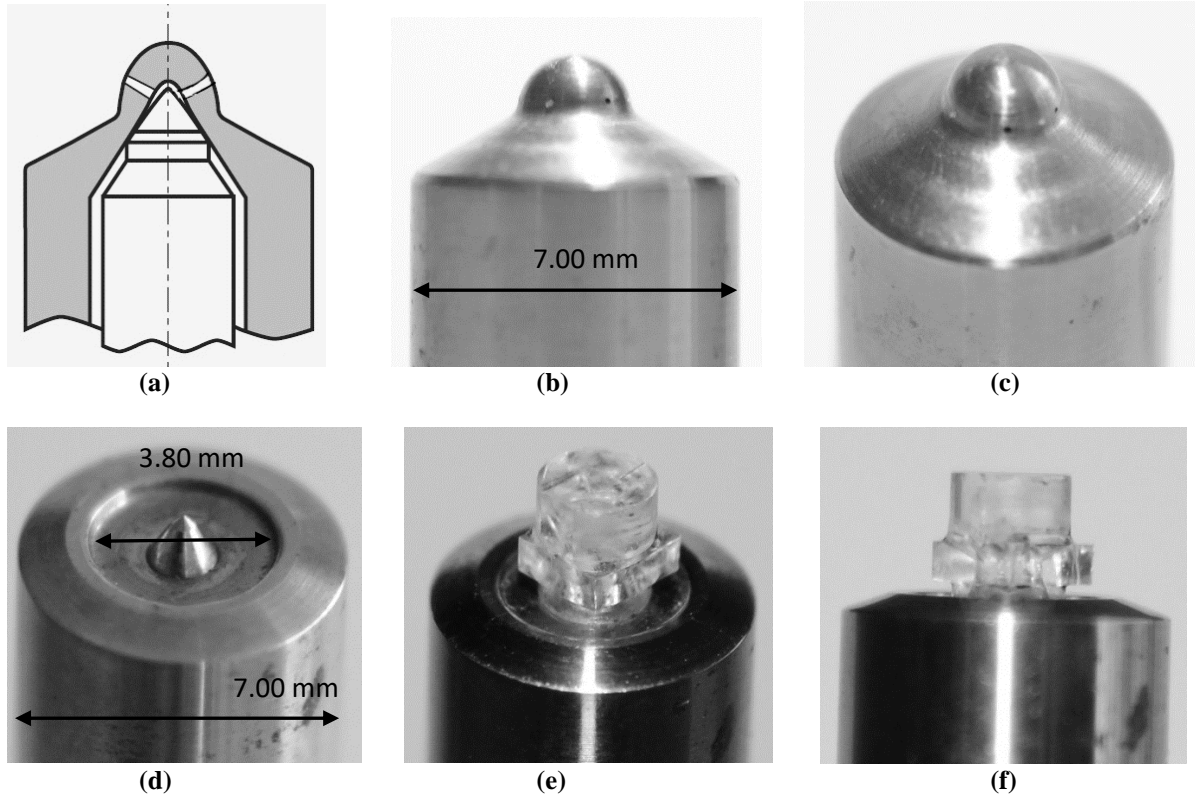
Figure 3: (a) Mini-sac nozzle concept, (b) side view of commercial 6-hole mini-sac nozzle, (c) inclined view of mini-sac nozzle, (d) inclined view of processed nozzle and sealed, internal needle, (e) inclined view of processed nozzle with acrylic mini-sac tip, and (f) side view of processed nozzle with acrylic mini-sac tip.
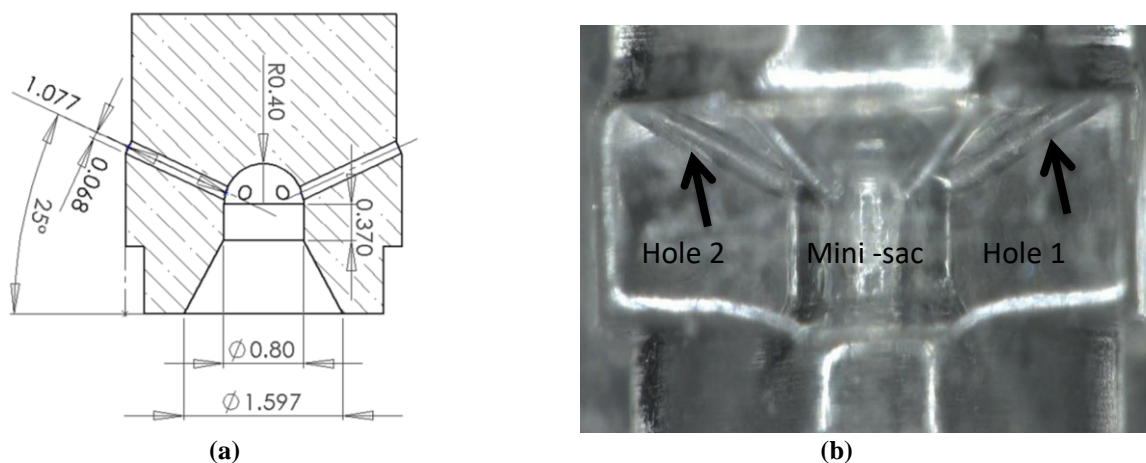
Figure 4: (a) Design schematic for optically accessible acrylic nozzle tip (measurements are in mm), (b) Nozzle interior image taken with a high magnification microscope. The arrows identify the holes of interest.

It was important to ensure that the nozzle tip was properly sealed to the injector body for the duration of the experiments. Consequently, a pneumatic air ram was mounted on the injector stand, which was attached to a balanced steel arm fitted with a fork containing an acrylic bar, that was employed to apply an axial force to a 35° angle fused silica cone.
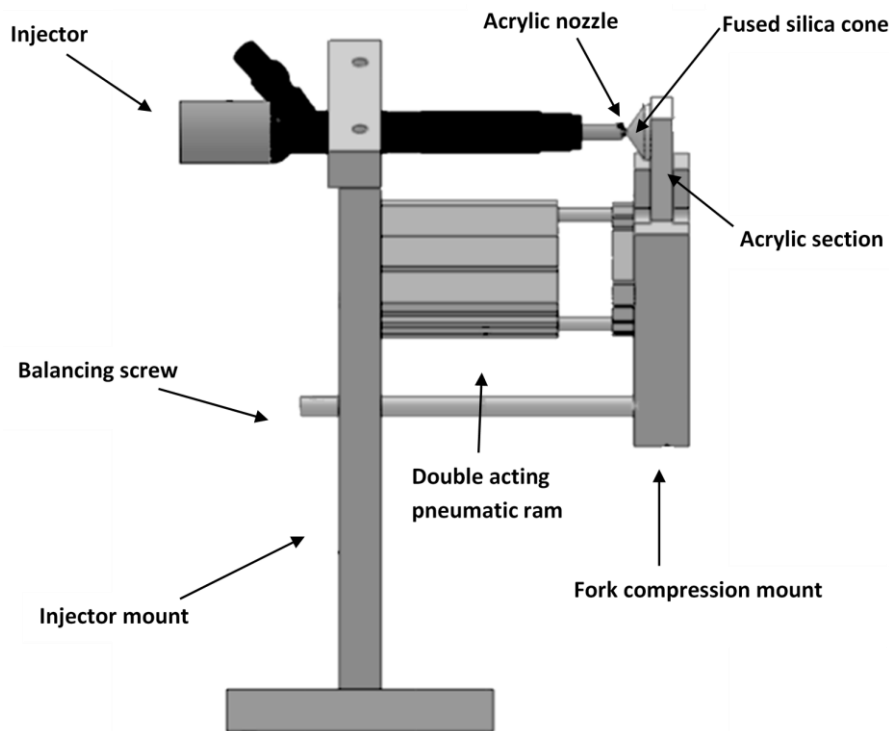
Figure 5: Schematic showing optically accessible injector assembly.

Figure 5 shows the pneumatic ram attached to the injector mount, supporting an aluminium fork, a rectangular acrylic section, and a fused silica cone, that provided the axial force required to seal the acrylic nozzle tip to the nozzle body. A precision balancing screw was located on the injector mount in order to balance the axial force provided by the pneumatic ram.

2.3 Optical Configuration

2.3.1 White Light and Camera Arrangement

Continuous white light obtained from a collimated Arri 400W POCKET PAR light source was passed through an infra-red filter, towards a 150 mm diameter, 500 mm focal length planar-convex lens. The converging light was then passed through a 50 mm diameter, 150 mm focal length bi-convex lens. The

focussed white light passed through the open centre of the spray extract assembly, the acrylic bar and the fused silica cone, forming a focus in the neighbourhood of the acrylic injector nozzle. A fraction of the white light scattered at 90° from the cavitating diesel fuel in the mini-sac and nozzle passages was captured on a high speed Photron FASTCAM SA1.1 camera using a Nikon 85 mm f/1.4 lens, reverse coupled to a 230 mm long extension tube. This arrangement (shown in Figure 5) enabled high resolution imaging of the field of view with a transverse spatial resolution of approximately 7.1μm/pixel.
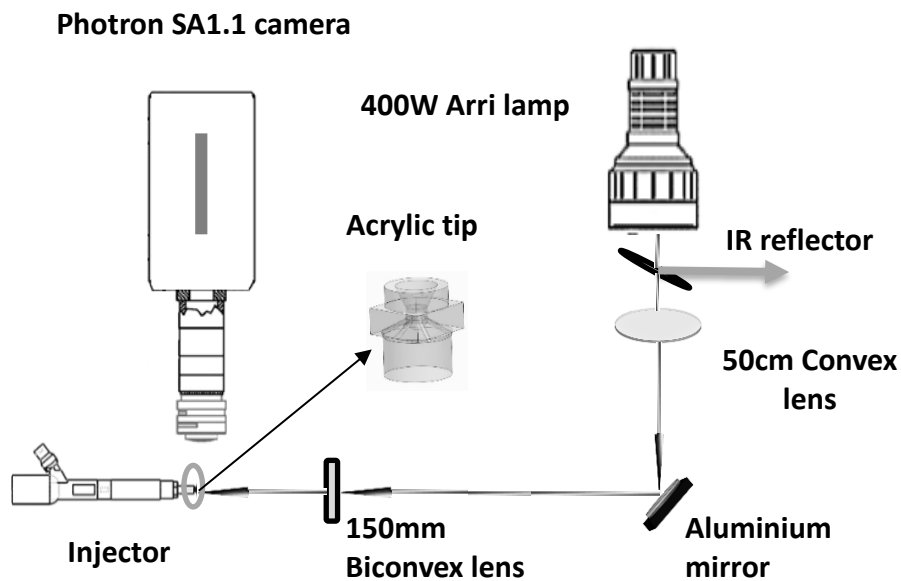
Figure 6: Schematic of the white light, injector and camera arrangement.

2.3.2   Timing and Method

The internal clock of the camera was synchronised to the 10 kHz clock provided by the customized injection timing box, which was in turn, synchronised to the 4.0 ms TTL injection pulse. This pulse was synchronised to the high pressure pump crank phase angle, ensuring that all injections occurred at the same position of the pump piston, thereby achieving a steady, repeatable injection-to-injection common rail pressure. The 4.0 ms TTL injection pulse was employed to trigger the fuel injection and the camera recording, and was itself recorded using a PC National Instruments data acquisition system.

The Photron SA1.1 camera was controlled by pc-based control software, which set: (1) external synchronization, (2) exposure duration, (3) external triggering, (4) dynamic range (12 bit), (5) number

of frames to record, and (6) file type (lossless 16-bit TIFF). The camera was configured to obtain

images with an exposure duration and frame rate of 1.0 µs and 10 kHz respectively, with the lens

aperture set at f/2. This arrangement facilitated real-time video capture of the internal nozzle flow. On

receipt of the trigger pulse, the camera took 150 image frames at 10 kHz frame rate in order to capture

the flow developing in the mini-sac and the nozzle holes. This arrangement obtained approximately 14

image frames prior to injection, 50 image frames during injection and 86 image frames after the end-

of-injection. Each data set was comprised of 50 injections at a rate of approximately 3 Hz to 5 Hz.

Following the acquisition of a data set, a set of background images were obtained. For this study, the

86 image frames of the post-injection mini-sac and nozzle hole flow were subjected to digital image

analysis for each of the 50 injections per data set.

2.4   Diesel Fuel

A crude oil derived, unadditized, middle distillate diesel fuel sample was provided by Shell Global

Solutions for this study, which was conducted with common rail pressures of 250 bar and 350 bar

respectively. The diesel sample had a distillation profile ranging from 172 °C to 342 °C, with a density

and kinematic viscosity of 825 kg/m^3 and 2.078 mm^2/s respectively.   Its physical properties are

summarized in Table 1, and its distillation curve is shown in Figure 7. This diesel fuel sample is referred

to as Fuel A in Figure 16.

Table 1: Physical properties of the diesel fuel under examination.

| Fuel type	Fuel description	Density @ 40ºC (kg/m^3)	Surface tension (N/m)	Kinematic Viscosity (m^2/s)
Diesel	Unadditized middle distillate diesel (172 ˚C – 342 ˚C)	825	0.03139	2.078 x 10^{-6}
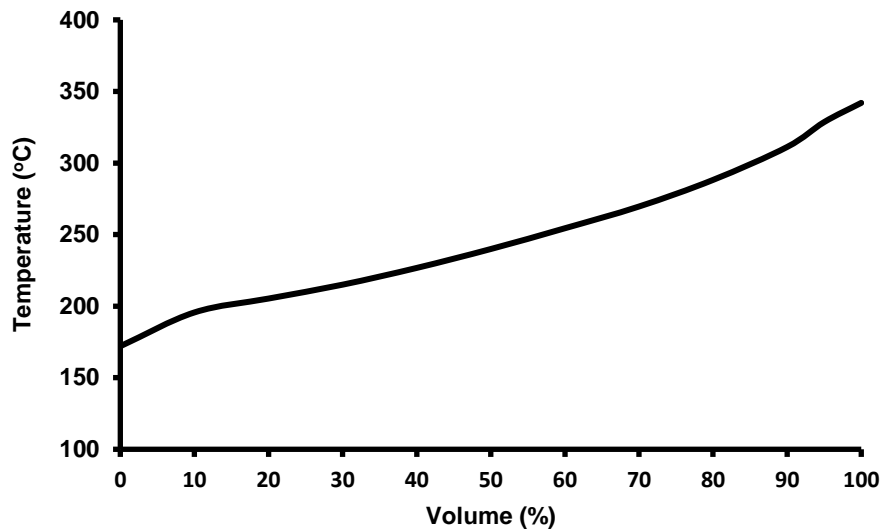
Figure 7: Distillation profile of unadditized, middle distillate diesel employed in this study.

3. Data Analysis

3.1 Mini-Sac Bubble Formation

The post-injection diesel fuel flow occurring in the nozzle mini-sac was subjected to analysis in order to obtain the size and pressure distribution of the bubbles that were formed. For this case, a MATLAB script was written to measure bubble radii forming in the mini-sac following the end-of-injection (EoI) for a subset of 20 injections. Initially, the background was subtracted from the raw image frames. These image frames were then subjected to homomorphic filtering to correct the signal bias caused by non-uniform illumination. Following this, the signal contrast of each image was enhanced to highlight the areas producing intense scattering which corresponded to the vapor structures being investigated. The script code detected the local maxima in terms of signal intensity. This was followed by a scan of the neighbouring pixels surrounding every local maximum to where the intensity reached 30% of the intensity of the local maximum; hence the detection of the boundaries of the objects was assessed to be accurate to 1.0 pixel uncertainty. Therefore the bubbles' boundaries were well defined, and the determination of their surface areas was considered to be accurate with an uncertainty of 1.0 pixel^2. The images of the mini-sac bubbles were circular, and so the bubbles were considered to be spherical; therefore the calculation of the surface areas and of the corresponding radii was calculated using Equation (1).

$$A = \pi r^2 => r = \sqrt{\frac{A}{\pi}}, \tag{1}$$

where *A* was the projected object surface area, and *r* was the corresponding radius of the bubble. The transverse spatial resolution of the camera and optics was 7.1 μm/pixel. Therefore the radii of the bubbles were converted from pixels to micrometers (μm). Finally, the simplified version of the Laplace-Young equation (Equation (2)) was employed to determine the pressure difference of the bubbles observed in the nozzle mini-sac, relative to the ambient pressure of the remaining fuel liquid.

$$\Delta P = \frac{2\gamma}{r}, \tag{2}$$

where *ΔP* is the bubble pressure difference (kPa), γ is the surface tension (N/m), and *r* is the radius of the bubble (μm). Finally, histograms of normalized frequency versus bubble radius and pressure difference comprised of 25 decades were produced describing bubble radii and pressures between 8 μm and 250 μm, 0.15 kPa and 15 kPa respectively over 50 injections.

3.2 Nozzle Mini-sac Flow

The mini-sac and nozzle flow analysis was conducted following the end-of-injection for all injections. The fuel injection was completed approximately 5.8 ms to 6.0 ms after the Start-of-Injection (SoI) trigger. Hence the duration of the fuel injection process was approximately 4.6 ms. At the instant of the needle return and reseal, vapour clouds and bubbles were observed to form inside the mini-sac, and bubbles/vapour capsules in the nozzle holes. The process of post-injection mini-sac bubble cloud and bubble formation is shown in Figure 8. The green, red and yellow lines in the Figure show the approximate locations of the mini-sac boundary wall, the tip of the injector needle, and the opposed view nozzle hole passages. The vapour cloud and bubbles forming in the mini-sac following the end-of-injection were visible as they scattered light elastically, which were captured on the camera sensor as the discrete objects in the mini-sac that produced optical scattering.
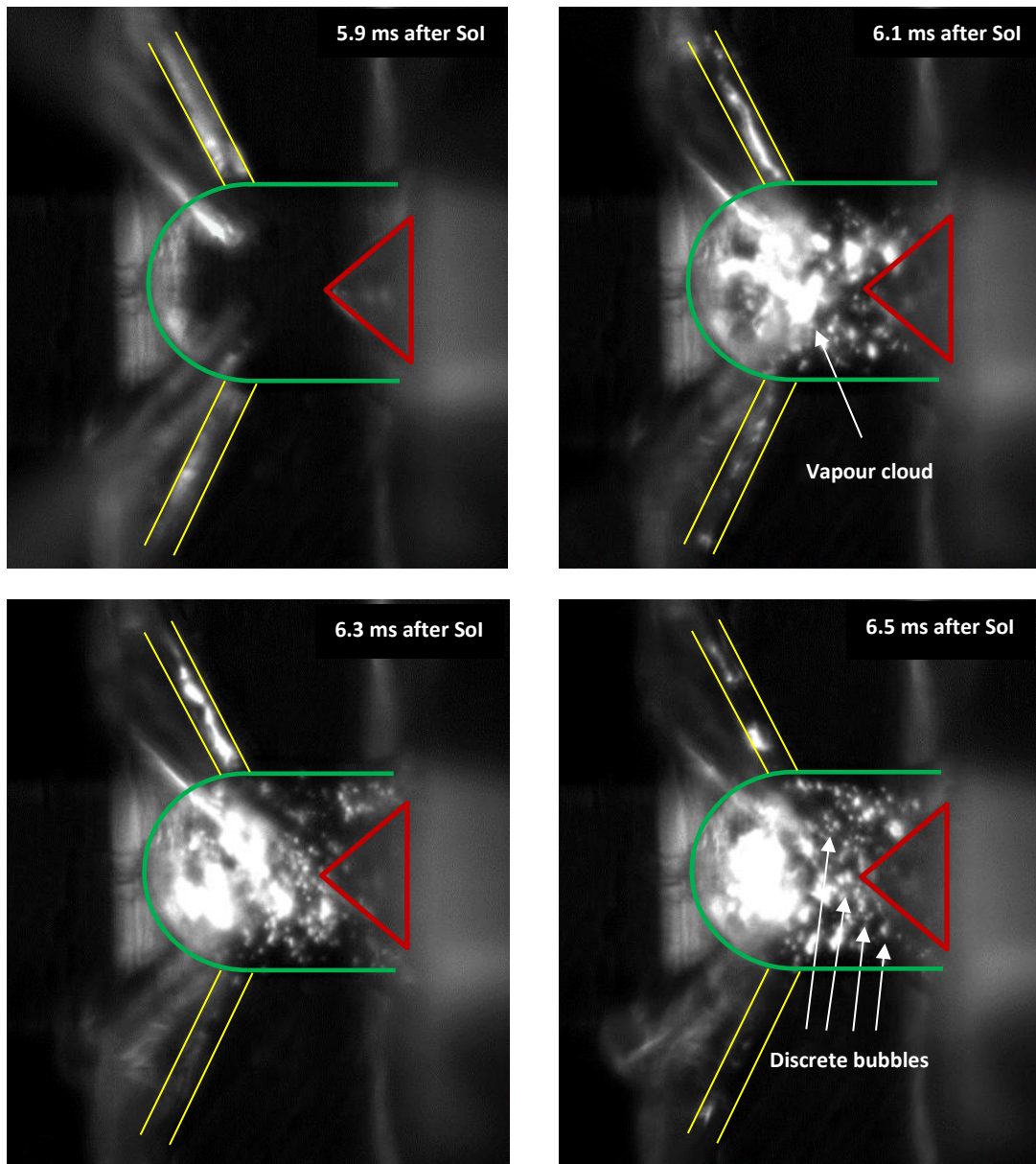
Figure 8: Image frames obtained from 5.9 ms – 6.5 ms after Start-of-Injection (SoI), showing the post-injection formation of a vapour cloud and bubbles in the mini-sac depicted by the bright spots occurring in the mini-sac due to elastic scattering of white light from the cloud/bubble surfaces.

After the needle returned to its sealed position, the flow developing in the mini-sac was fast and turbulent, which was difficult to track. The flow took approximately 1.1 ms to settle down, enabling bubble tracking. The bubble movement in the mini-sac was observed to settle down from its initially turbulent state into a slowly decaying, orderly rotational motion, reflecting the post-injection vorticity of the remaining diesel fuel. The position and motion of several bubbles were manually detected in a sequence of raw images obtained between 7.2 ms and 11.5 ms after the start-of-injection trigger. For convenience, the instant in time of needle reseal (End-of-Injection (EoI)) was the starting point of this

analysis (approximately 6.0 ms after Start-of-Injection (SoI)); thus frame 77 and frame 120 corresponded to 1.2 ms after EoI and 5.5 ms after EoI respectively.

Figure 9 (a) shows a conceptual view of the nozzle mini-sac from the bottom of the mini-sac towards the needle and nozzle base. Prior to any processing, the center axis of the nozzle was determined. The intersection point of this axis with the needle tip was chosen to be the origin. The figure identifies what was considered a clockwise and anti-clockwise circumferential flow direction. The figure also shows the trigonometric relations for a theoretical bubble moving circumferentially in an anti-clockwise sense with an initial radius R_0, located later at 3 different heights in the nozzle hole as viewed from the z-axis side (heights identified by y_1, y_2 and y_3).

Initially, the varying relative position of several bubbles was manually detected in a sequence of 44 image frames using Matlab. The varying coordinates of the rotating bubbles were saved in a spread-sheet for later processing. For example, the location of two bubbles in a sequence of six image frames spaced at 0.2 ms intervals is shown in Figure 9 (b). The distance R_0 was the distance between the center axis and the point which passed though line AB once at least. It was necessary to begin tracking the bubble either from point A or B, because at these points the angle θ was known to be equal to $-\frac{\pi}{2}$ or $\frac{\pi}{2}$ respectively. The azimuthal angle of the i'th bubble relative to the central axis θ_{ij} corresponding to frame j was determined using Equation (3).

$$\theta_{ij} = sin^{-1}\frac{y_{ij}}{R_0},$$ (3)

where y_{ij} was the y-coordinate of the i'th bubble in the j'th image frame.

The term y_{ij} changed from frame to frame but the R_0 was assumed constant. This was due to the assumption that the bubbles moved circumferentially in the sac, based on the observation of the settled motion of the bubbles (and surrounding liquid) following the end-of-injection. Unfortunately, the location of the camera prevented the measurement of radial motion within the mini-sac. The calculated

angles for every single bubble were used for the angular velocity (Ω) calculation. The expression used (Equation 4) to calculate the angular velocity of the *i*'th bubble at frame *j* is

$$\Omega_{i,j} = \frac{\theta_{i,j+1} - \theta_{i,j}}{\Delta t} \,, \tag{4}$$

where Δt was the time interval between subsequent images ($\Delta t = 10^{-4}$ s).

For all injections, the position and motion of many bubbles were detected and tracked; therefore the overall angular velocity in the *j*'th frame of the *n*'th injection was the mean angular velocity determined over all of the tracked bubbles. This is expressed mathematically in Equation 5:

$$\bar{\Omega}_j^{(n)} = \frac{1}{N} \sum_{i=1}^{N} \Omega_{i,j}{}^{(n)} \tag{5}$$

The calculated mean angular velocity was then plotted versus time in order to determine the rate of change of the mean angular velocity of the bubbles over an injection event and finally, over a set of 20 injections. The mean angular velocity over 20 injections was obtained from Equation 6.

$$\bar{\Omega}_j = \frac{1}{20} \sum_{n=1}^{20} \bar{\Omega}_j^{(n)} \tag{6}$$

where *n* is the injection number.

(a)
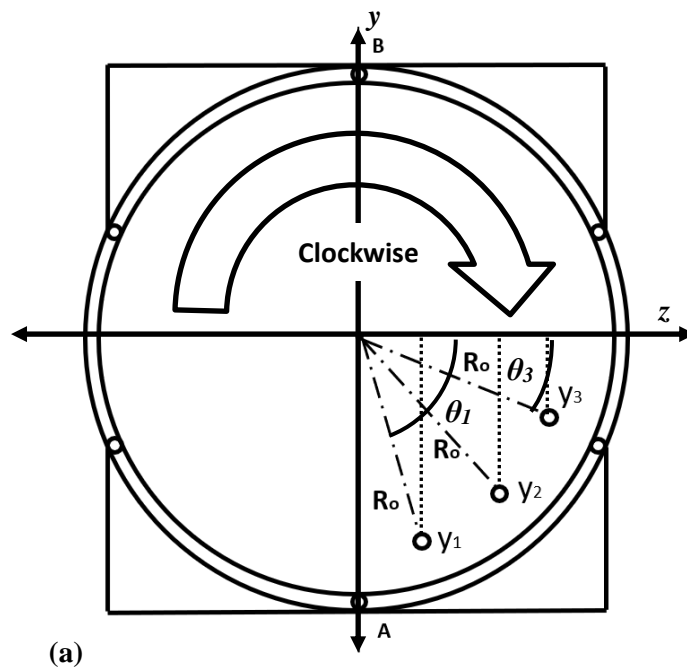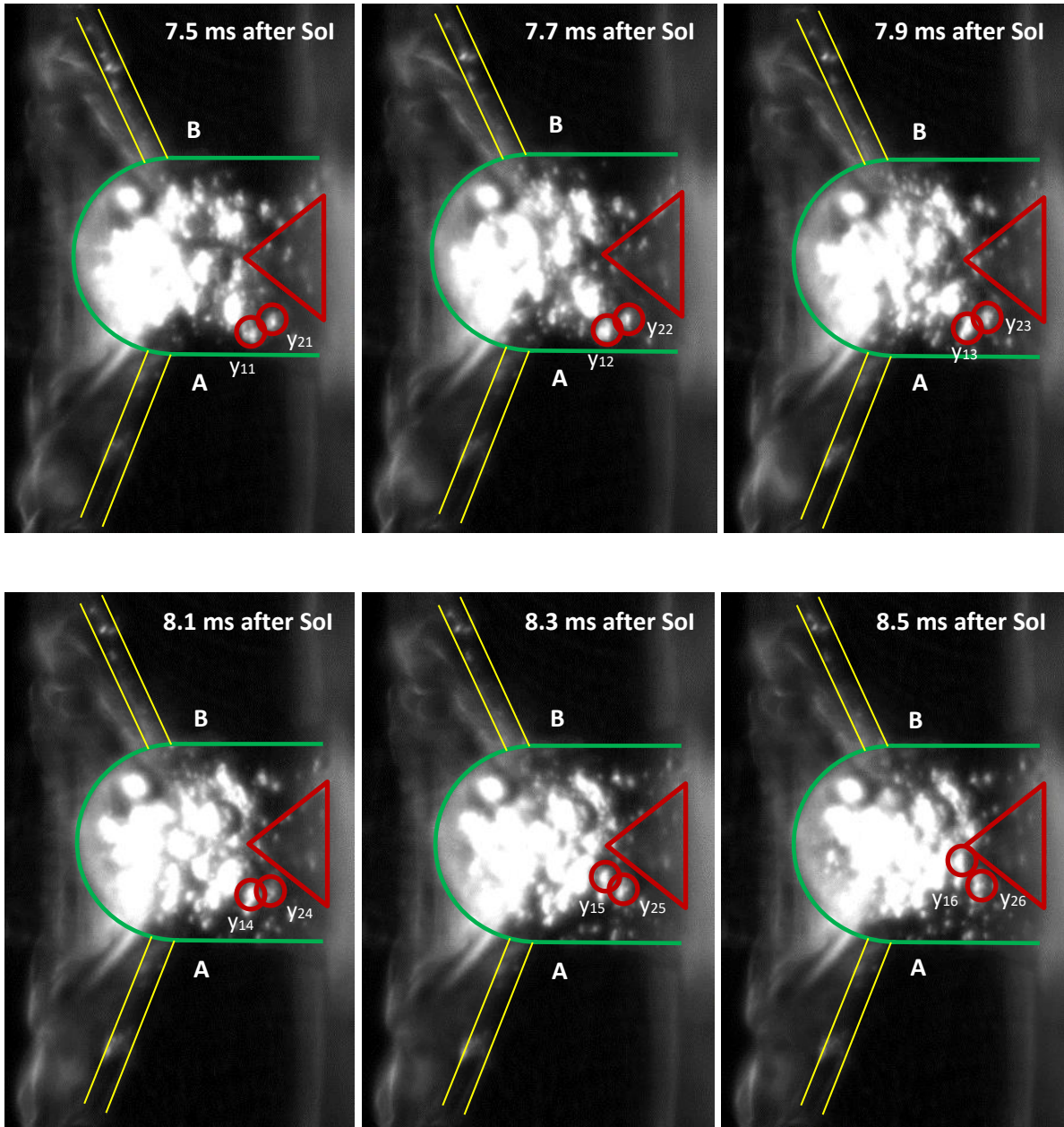
(b)

Figure 9: (a) Representation of tracking process of an individual structure. y_1 to y_3 are the y-co-ordinates in three successive frames (nozzle view from the bottom), (b) an example of bubble tracking in a series of raw images (the red circles indicate the bubbles of interest).

3.3 Nozzle flow

Bubbles and/or vapour capsules were observed to appear and move in the nozzle holes following the end-of-injection. This was considered to be connected to the circumferential flow observed inside the mini-sac. Figure 10 is a sequence of 4 image frames that show bubbles moving outwards due to the post-injection nozzle flow (~ 5.8 ms after the injection trigger signal); in many cases though the bubble

motion was altered and the detected structures were observed to move inwards towards the mini-sac. After the needle re-sealed at approximately 6.0 ms after SoI, any other bubble appearance was a result of bubbles either flowing from the mini-sac into the holes, or a phase discontinuity occurring at the head of the liquid diesel in the nozzle, permitting external gas access to the interior of the nozzle holes.
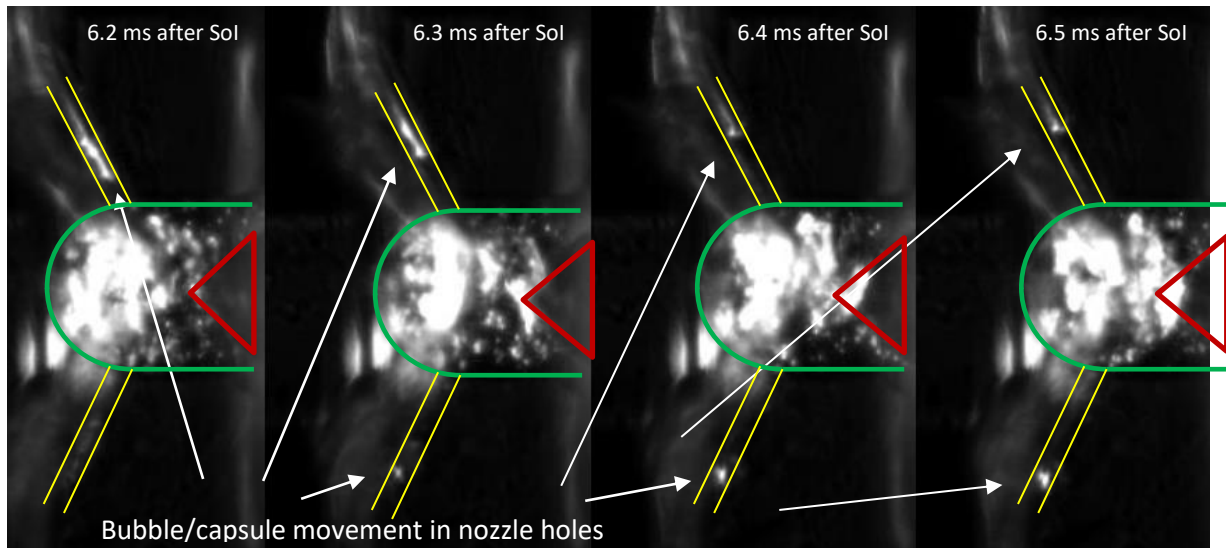

Figure 10: Successive image frames showing the initial motion of bubbles/capsules in both upper and lower nozzle holes (6.2 ms – 6.5 ms after SoI) being outward.

The detection of the nozzle fluid motion was achieved employing a Matlab script that detected either the centre of an individual bubble, or the centres of the front and rear interfaces of vapour capsules. Initially, the background image was subtracted from the raw image and a global threshold employed to eliminate the noise contained in the image. Following this, the contrast of each image was enhanced to highlight the bright scattering areas which corresponded to the objects under examination. The coordinates of the detected objects were employed to determine the displacement of the bubble over a set of successive image frames. In this regard, the entrance of the nozzle hole was chosen to be the reference point. The displacement Δl was defined to be the distance between the location of the bubble in each image and the reference point (Equation 7). The calculated distance was then converted into mm (transverse spatial resolution was 7.1 μm/pixel) and displacement versus time graphs plotted. The maximum displacement on the displacement axis of the graph corresponded to the 1.1 mm length of the nozzle hole. Any change in the sign of the slope of the graph indicated a reversal in the bubble direction

of travel. A positive slope corresponded to outwards bubble movement, whereas a negative slope to an inwards movement.

$$\Delta l = \sqrt{(x_1 - x_o)^2 + (y_1 - y_o)^2} \tag{7}$$

where x_1 and y_1 were the X and Y coordinates of the bubble respectively, and x_0 and y_0 were the X and Y coordinates of the reference point respectively.

## 4. Results and Discussion

4.1 Post-Injection Vapour Cloud Formation in the Mini-Sac and Vapour Capsule Formation in the Nozzle Holes

The internal flow analysis was focused on phenomena occurring after the end-of-injection (EoI). When the needle re-sealed at the end-of-injection, a vapour cloud and bubbles were observed to form in the mini-sac which were not present during the injection. The formation of the vapour cloud and bubbles was caused by the short duration decrease in pressure occurring in the mini-sac and nozzle holes following injector needle reseal. The decrease in local fluid pressure to near vacuum conditions occurred as a result of post-injection fuel liquid vacating the mini-sac and nozzle holes downstream of the needle through the inertial effects of the large pre-reseal fluid momentum. The formation of the vapour cloud and discrete bubbles in the mini-sac, and the bubbles/capsules in the nozzle holes occurred because the inertial transport and evacuation of fuel liquid from the mini-sac and nozzle holes produced local fluid pressure that fell below the saturated vapour pressure of the diesel, enabling the formation of vapour cavities within the remaining liquid [38].

Figure 11 shows 9 image frames at 0.2 ms intervals, spaced around the instant of needle reseal that marked the end-of-injection (5.8 ms after SoI). The image data shown was obtained for an accumulator pressure of 250 bar. The first image frame in the sequence (frame marked 5.7 ms after SoI) shows that there were no vapour clouds present in the mini-sac prior to the end-of-injection, and a cavitating flow occurring in the nozzle holes during the injection. However, the image frames captured 0.1 ms and 0.3 ms after the end-of-injection (frames marked 5.9 ms after SoI and 6.1 ms after SoI) shows the formation and growth of a vapour cloud in the mini-sac and vapour capsules/bubbles in the nozzle holes.

The momentum-driven fuel liquid evacuation of the nozzle holes immediately following the end-of-injection permitted the formation of vapour capsules that were able to extend over the full length of the nozzle holes. The image frames marked 6.5 ms and 6.7 ms after SoI in Figure 11 show this effect in the bottom hole. The rapid decrease in fluid pressure in the mini-sac and nozzle holes to below the gas pressure at the exit of the nozzle holes produces a pressure rarefraction and an inward flow in the nozzle holes towards the mini-sac. Post injection fuel liquid films or droplets forming on the external surface of the injector nozzle in the neighbourhood of the nozzle hole exits are able to be sucked back into the nozzle holes. This is observed in the bottom nozzle hole passage in Figure 11, in image frames marked 6.9 ms, 7.1 ms and 7.3 ms after SoI.

The post-injection formation of the low-pressure vapour capsules in the nozzle holes permits external gas to enter the nozzle hole and mix with the fuel vapour in the nozzle hole during the pressure rarefraction that occurs once the nozzle holes have been vacated of fuel liquid.
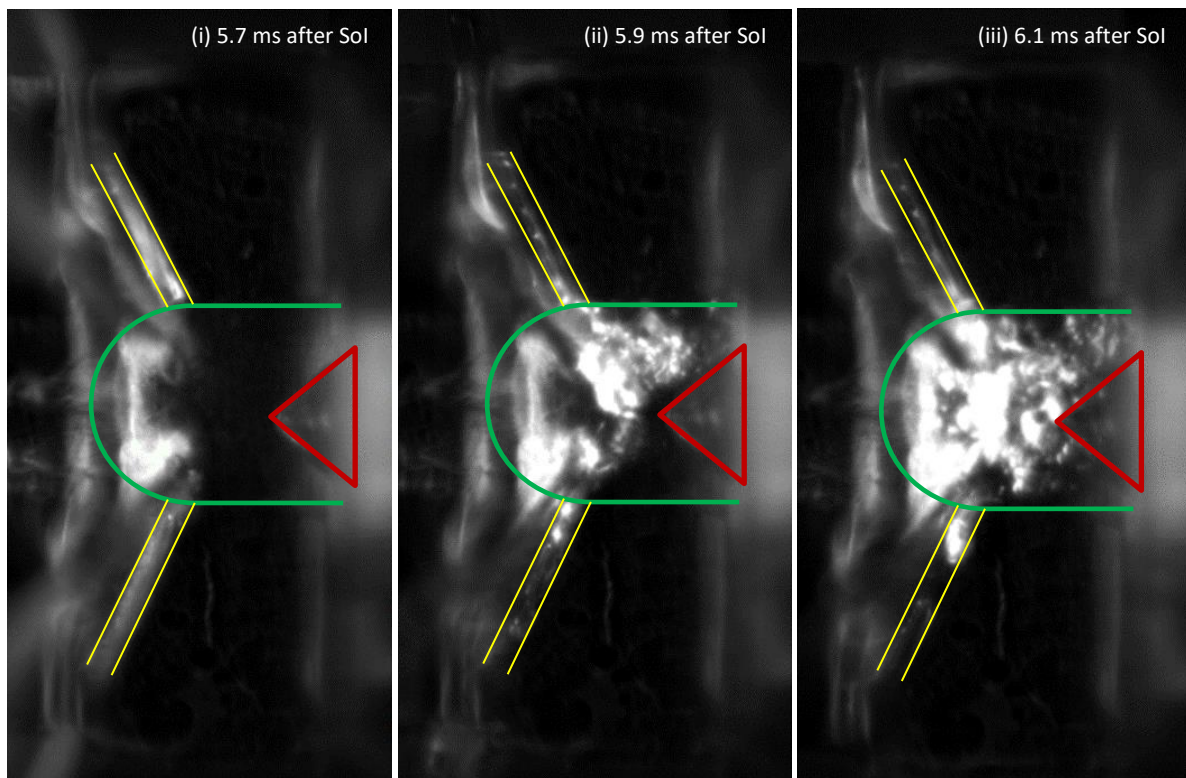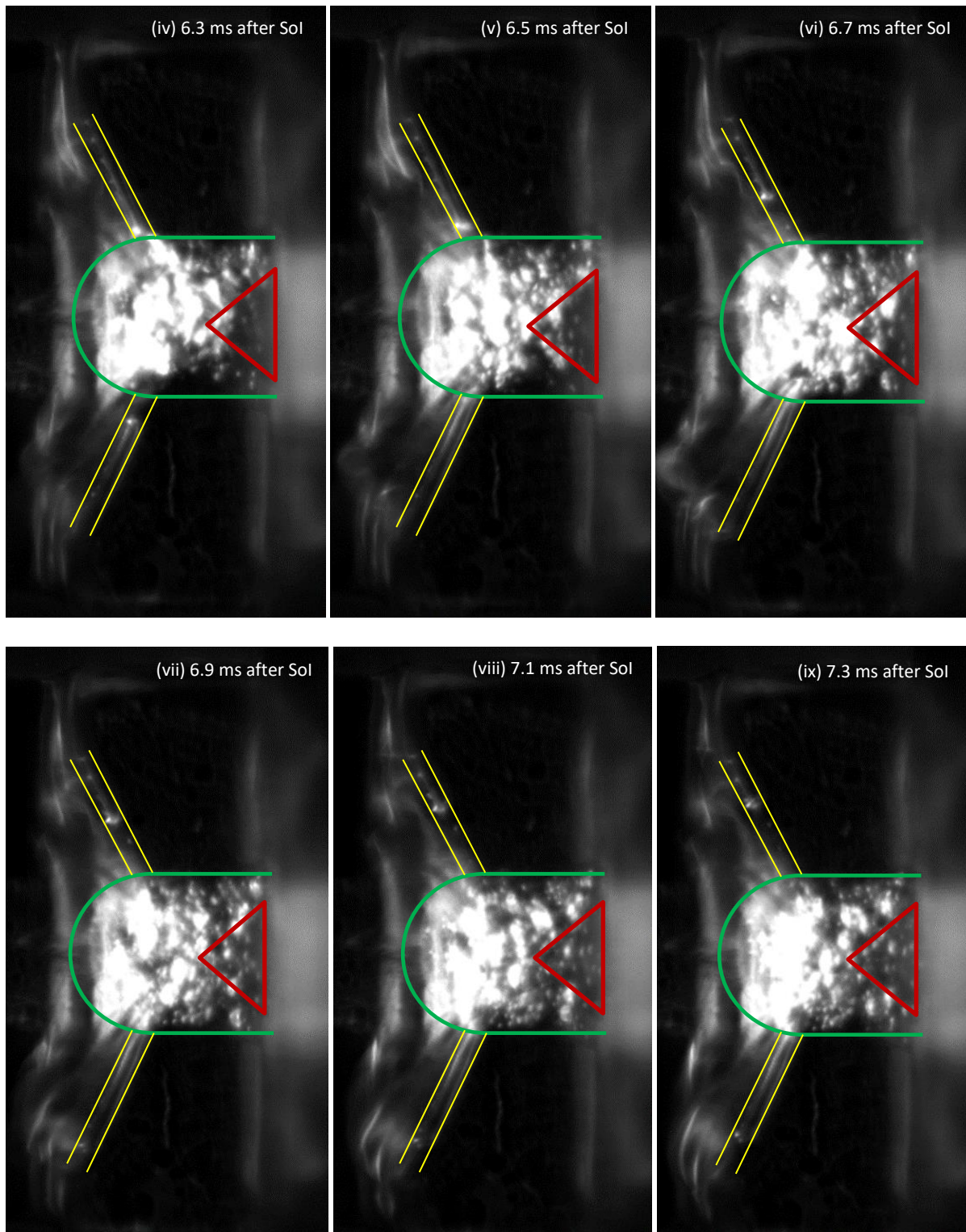
Figure 11: 9 image frames showing vapour cloud formation in the mini-sac, and vapour capsule formation in the nozzle holes following the End-of-Injection at 5.8 ms.

4.2 Post-Injection Mini-sac Diesel Flow Vorticity

Discrete bubbles were observed to be transported around the mini-sac and in the nozzle holes as a

consequence of the residual motion of the diesel liquid remaining in the mini-sac and nozzle holes.

The motion of the bubbles in the mini-sac was initially unsteady and of large velocity and turbulence intensity following the end-of injection, taking approximately 1.1 ms to settle to a steady rotational motion that enabled bubble tracking. The rotational motion of the fluid was assumed to be circumferential which had large initial angular velocity, which was observed to quickly decrease due to the flow shear imposed by the stationary mini-sac boundary wall.

In Figure 8 above, the green, red and yellow lines show the approximate location of the mini-sac boundary walls, the needle tip and the opposed nozzle passages respectively. Moreover, at 5.9 ms after SoI no bubbles were present inside the sac volume, whereas in the following image frames (6.1 ms – 6.5 ms) they appeared due to the pressure drop following the momentum-driven fuel liquid evacuation of the mini-sac. The bubbles were seen as the strongly scattered white light structures due to the light scattered from their surfaces. The number of bubbles formed inside the mini-sac volume was observed to increase significantly after the needle re-sealed at the end-of-injection (5.8 ms after SoI). For convenience, the instant when the needle re-sealed was set equal to 0.0 ms for the remainder of this analysis.

The unadditized middle distillate diesel fuel was employed for the examination of the decay of the rotational flow inside the nozzle mini-sac at 250 bar and 350 bar rail pressures. Figures 12 (a) and (b) show the decay of the mean angular velocity of the diesel in the mini-sac following the end-of-injection (EoI) plotted against time at 250 bar and 350 bar accumulator (common rail) pressure, averaged over 20 injections. The error bars show the range of variation (1 standard deviation) of the instantaneous mini-sac fluid angular velocities measured from injection to injection over 20 injections.

(a) Post-injection mini-sac fluid angular velocity (250bar, inj.1-20)

(b) Post-injection mini-sac fluid angular velocity(350bar, inj.1-20)

(a)   **(b)**
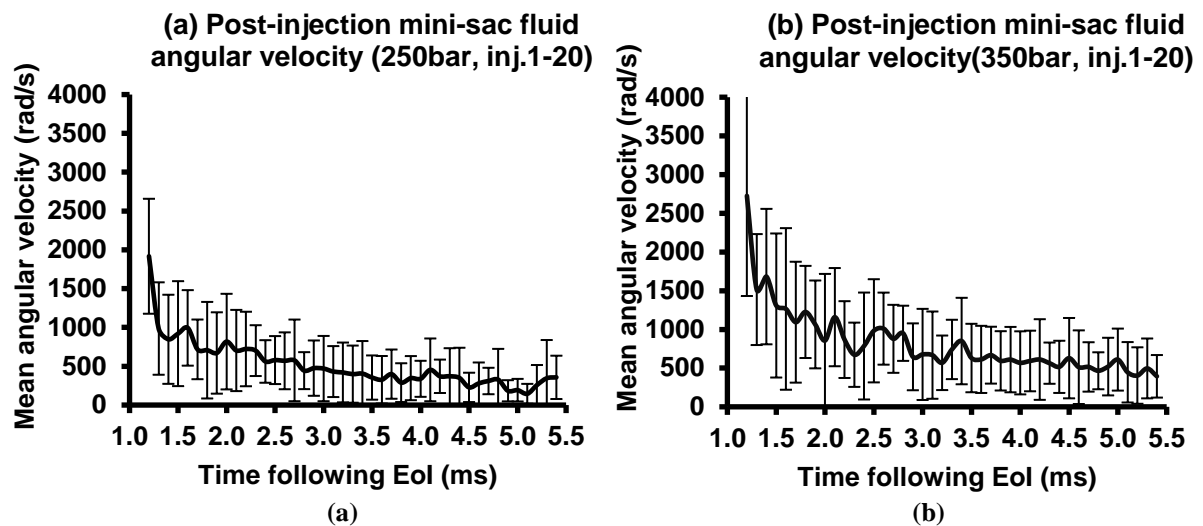
Figure 12: Graphs showing the decay in mean post-injection mini-sac fluid angular velocity with time following end-of-injection for (a) 250 bar, and (b) 350 bar accumulator pressure. The error bars show the 1σ variation in measured instantaneous angular velocity over 20 injections.

Figure 12 (a) and (b) suggests a correlation between the mean decay rates of the fuel angular velocity as a function of rail pressure. In particular, the initial angular velocity of the diesel fuel at 250bar (Figure 12 (a)) was observed to be significantly lower than that occurring at 350 bar (Figure 12 (b)). This finding is attributed to the increased angular momentum of the fuel flow occurring in the injector fuel galleries and across the nozzle-needle annulus due to the increased rail pressure. However, the vorticity decay rates for the two cases were similar, suggesting that an increase in rail pressure did not have a significant effect on the post-injection vorticity decay rate. It is believed that the post-injection dynamics of the flow in the mini-sac do not change fundamentally with increasing rail pressure, apart from the effect of rail pressure on post-injection vorticity (angular velocity). The large scattering intensities being generated by the bubble cloud and the bubbles in the mini-sac volume created large saturation regions as can be observed in Figures 8, 9 and 10; thus the bubbles were not always well-defined, and they could not always be tracked for the whole duration of the post injection flow. Therefore, fluctuations in the mean angular velocity could be seen in Figures 12 (a) and (b).

Table 2 shows the relative percentages of clockwise, anti-clockwise and irregular motion obtained by the diesel in the mini-sac following the end-of injection. The direction of fluid motion was defined by the view obtained at the bottom of the nozzle tip towards the injector and needle. The table shows that the flow obtained at 350 bar accumulator pressure was anti-clockwise for 92% of injections, and

irregular (undeterminable) for the remaining 8% of injections. This is to be contrasted with the measurements made at 250 bar, which show that the flow was anti-clockwise for 80% of injections, clockwise for 4% of injections, and irregular (undeterminable) for 16% of injections.

Table 2: Statistics of the mini-sac flow direction for diesel fuel obtained in the mini-sac after the end-of-injection at 250 bar and 350 bar accumulator pressure (Nozzle A).

Accumulator Pressure (bar)	Clockwise (%)	Anti-clockwise (%)	Irregular (%)
250	4	80	16
350	0	92	8

4.3 Mini-sac Bubble Formation

The determination of the bubble sizes inside the nozzle mini-sac and the resulting pressure differences, as a function of rail pressure, potentially provides useful information on the composition of the bubbles inside the nozzle mini-sac. The substance inside the nozzle mini-sac would be expected to be comprised of diesel liquid and vapour; however this cannot be true in real systems, due to the mixing and dissolution of air (oxygen and nitrogen) in the fuel that occurs in the fuel tank, the priming pump and the metered main pump.

The momentum-driven evacuation of liquid fuel in the mini-sac that followed the re-seal of the injector needle at the end of injection was responsible for vapour cloud formation in the mini-sac and vapour capsule/bubble formation in the nozzle holes. The formation of the vapour cloud and bubbles produces large concentration gradients at the phase boundaries, which support the evaporation of oxygen and nitrogen molecules out of solution, thereby producing bubbles comprised of fuel vapour, containing oxygen and nitrogen gases. The simplified version of the Young–Laplace equation (Equation 2) was used to calculate the gas/vapour pressure of the bubbles in the mini-sac relative to the surrounding liquid pressure. According to this equation, the pressure difference between the bubble gas/vapour and the surrounding liquid is directly proportional to the surface tension and inversely proportional to the

bubble radius. Figures 13 and 14 show the bubble diameter and bubble-to-liquid pressure difference normalized frequency distributions for the diesel fuel in the range of diameters and pressure differences of 8.0 μm to 150 μm, and 0.15 kPa to 15 kPa respectively, at 4 different times following the End-of-Injection (EoI, instant of needle re-sealing), (0.1ms, 0.8ms, 2.5ms, and 5.5ms after EoI) over 20 injections at 250 bar and 350 bar common rail pressure.
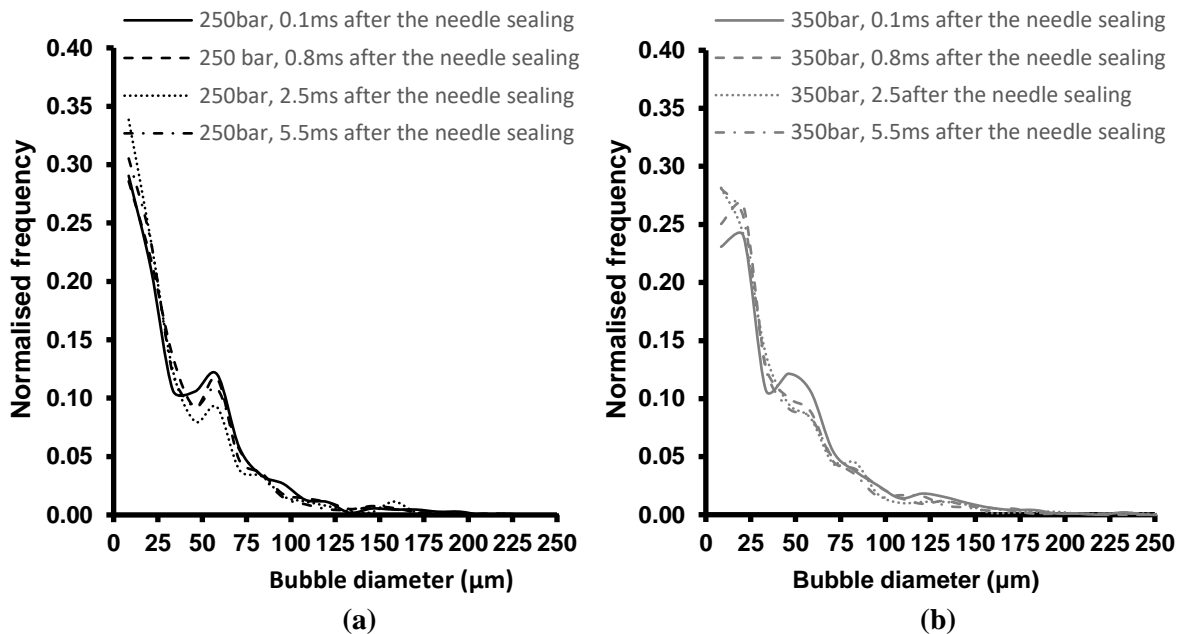

Figure 13: Bubble size distributions at 0.1ms, 0.8ms, 2.5ms and 5.5ms after the end-of-injection (EoI) for 20 injections at (a) 250bar and (b) 350 bar.

The black and gray lines and bars shown in the charts correspond to measurements at 250 bar and 350 bar rail pressure respectively, while the solid, dashed, dotted and dashed-dotted lines and bars correspond to 0.1ms, 0.8ms, 2.5ms, and 5.5ms after the end-of-injection respectively. In particular, Figures 13 (a) and (b) show that the bubble sizes do not change significantly during the post injection mini-sac fluid flow for both 250 bar and 350 bar accumulator pressures. This finding suggests that (1) the bubbles remain relatively stable during the post-injection period, and (2) the dynamics of the flow effectively remains the same; i.e. once the flow has settled down, the flow dynamics were observed to be independent of the rail pressure. This is due to the fuel pressure in the nozzle mini-sac settling down to a steady value independent of the accumulator pressure following the end-of-injection.

A comparison of Figures 13 (a) and (b) reveals that the distribution of bubble diameters formed following the injections at 350 bar rail pressure is very similar to the corresponding distribution of bubble diameters obtained following the injections at 250 bar rail pressure. This is unsurprising, since these bubbles were formed out of the liquid during the low fluid pressure that followed the momentum-driven liquid fuel evacuation of the mini-sac and nozzle holes following the re-seal of the injector needle at the end-of-injection.


(a)   (b)
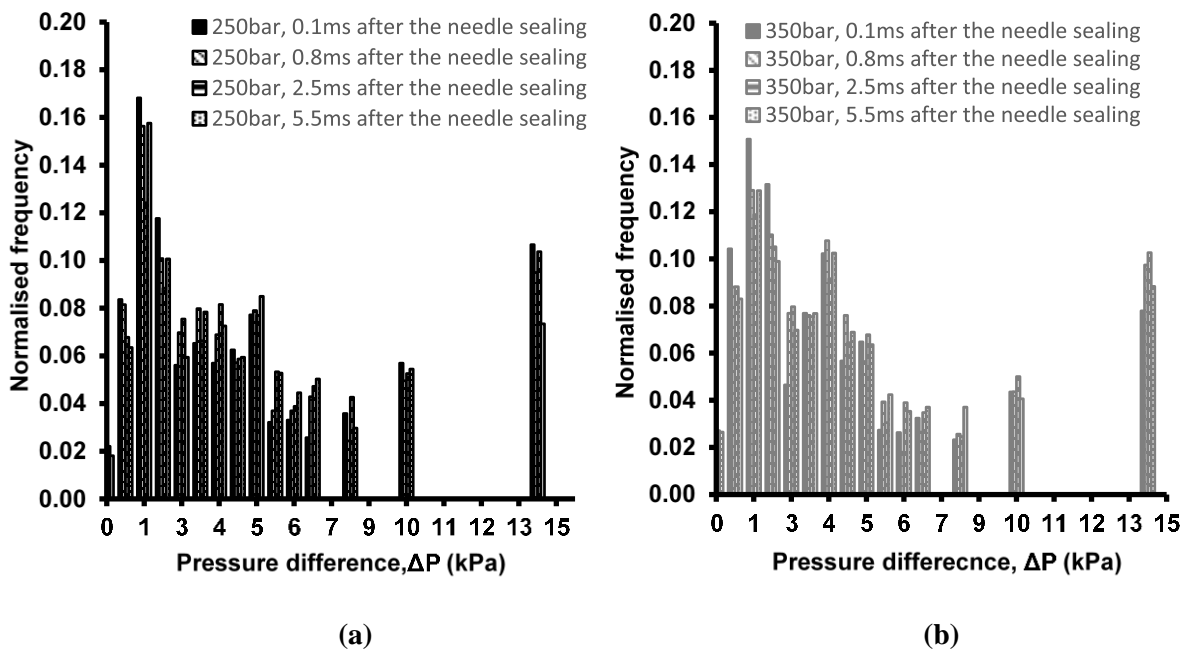
Figure 14: Pressure difference distribution at 0.1ms, 0.8ms, 2.5ms and 5.5ms after the end-of-injection for 20 injections at (a) 250bar, and (b) 350 bar.

Figures 14 (a) and (b) provide supporting evidence for the presence of oxygen and nitrogen in the bubbles and the fuel as the pressure differences range between 0.15 kPa and 15 kPa. If the fuel in the mini-sac consisted of diesel fuel only, the pressure differences across the bubble interfaces should be much lower, as the saturated vapor pressure of conventional diesel lies in the range of 0.01 kPa – 0.05 kPa [39].

4.4 Post-Injection Fuel Nozzle Flow

In the period following the end of injection, bubbles and/or vapour capsules were observed to appear in the nozzle holes. These were formed through a combination of the completion of the multi-phase cavitating flow occurring in the nozzle holes during injection, and the low fuel pressure formed behind

the momentum-driven evacuation of fuel liquid from the mini-sac and the nozzle holes following the end-of-injection. Figure 10 shows a succession of four image frames of a vapour capsule that has formed in the upper nozzle hole following the end-of-injection. These bubbles and/or vapour capsules were observed to either remain stationary, or travel towards or away from the mini-sac. The momentum-driven liquid fuel evacuation of the mini-sac and nozzle holes following the end-of-injection, together with the retained fuel mass, specifies the post-injection mini-sac fluid pressure. In many cases, this will be lower than the external gas pressure, resulting in a fluid force acting along the axes of the nozzle holes towards the mini-sac. The response of the residual liquid and vapour remaining in the nozzle holes is to reverse the residual momentum-driven direction of motion towards the nozzle exit to an inward motion towards the mini-sac.

As the turbulent flow of the fuel remaining in the mini-sac settled down to a steadily decaying rotational flow (Figure 12), it is believed that the circumferential and radial motion of the fuel inside the mini-sac created varying pressure conditions at the entrances to the nozzle holes relative to the exits, causing the fuel and bubbles/vapour capsules to adjust their movement in the nozzle passages. In this, the combination of external gas pressure, mini-sac fluid pressure, and motion of the fuel in the nozzle mini-sac following the end-of-injection seemed to act like a pump, causing the liquid fuel and the imbedded bubbles to travel either toward the mini-sac or the passage exit. Figure 15 shows the change in displacement of a bubble imbedded in the lower nozzle hole as a function of time (defined by the 1.0 ms period between image frames). In Figure 15 a bubble was observed to move inwards towards the mini-sac due to the direction of the surrounding liquid flow (1.0 ms to 6.0 ms after the end-of-injection). The later motion of the fuel and bubbles in both holes were observed to be nearly synchronous with the settled rotational flow inside the mini-sac. It appeared that the fluid motion in the nozzle holes were correlated with the circumferential motion of the fluid in the mini-sac. Figure 16 shows an example of the post-injection motion of the fluid in the nozzle holes correlated with the circumferential motion of the fluid remaining in the mini-sac.
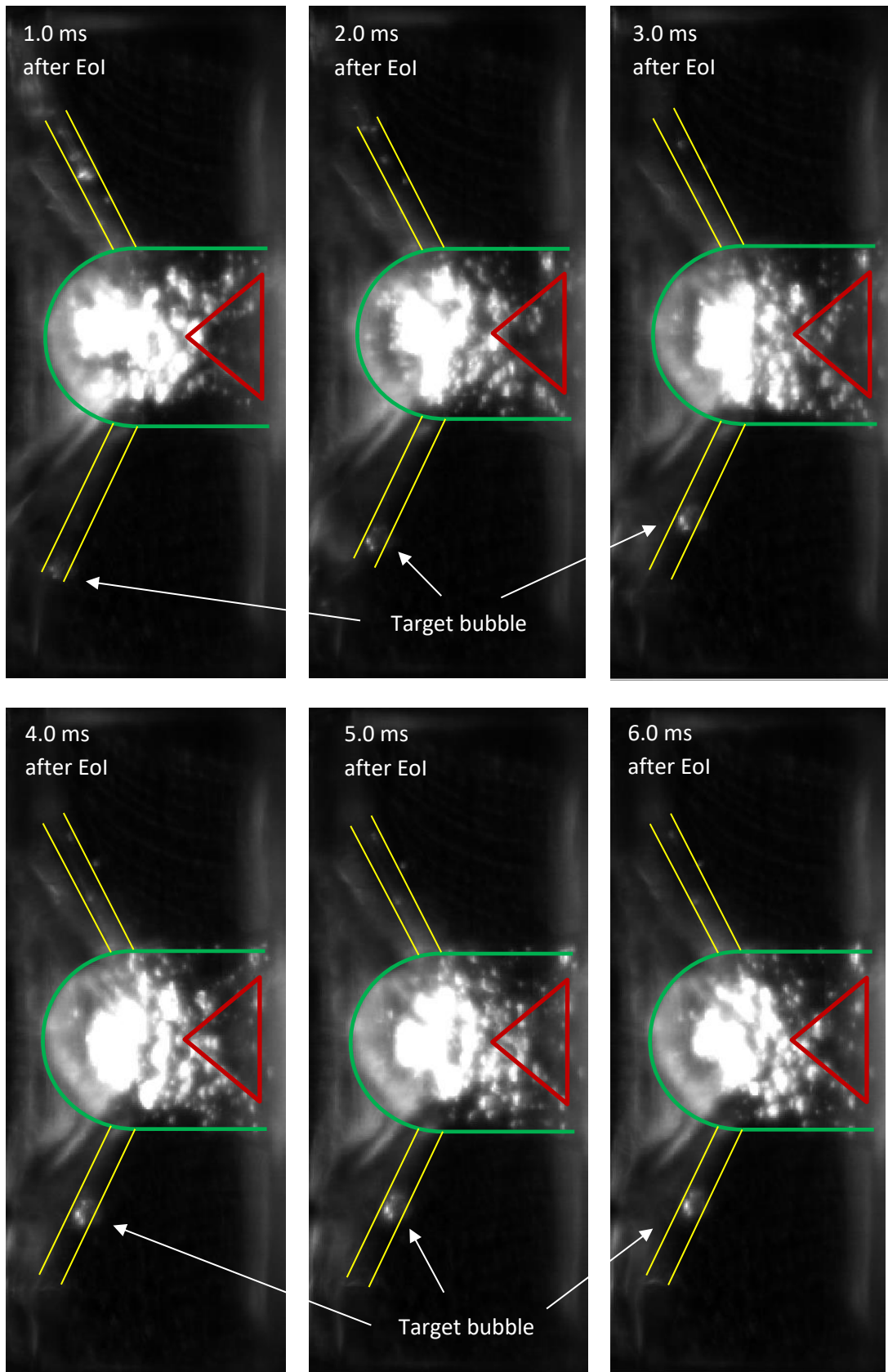
Figure 15: A sequence of image frames beginning 1.0 ms after the end-of-injection, obtained at 1.0ms interval between frames. A bubble is observed moving inwards towards the mini-sac in the lower passage.

Figure 16 shows a correlation between the fuel liquid/vapour velocities attained in the nozzle holes and the corresponding liquid fuel angular velocities obtained in the mini-sac following the end-of-injection, for 10 vapour objects (bubbles and vapour capsules) observed in the lower nozzle hole over 5 injections. In the figure, the reference to fuel A in the specification of the nozzle hole bubble/capsule velocity as plotted against mini-sac fluid angular velocity is an identification code of the unadditized, middle distillate diesel fuel employed in this investigation. The correlations lying between 0.35 and 0.74 (7 out of 10) provide some support to the argument that the rotational/radial motion of the diesel remaining in the mini-sac following end-of-injection produces local pressure gradients across the nozzle holes that results in applied forces and corresponding rates of change of diesel fluid momentum in the nozzle holes.
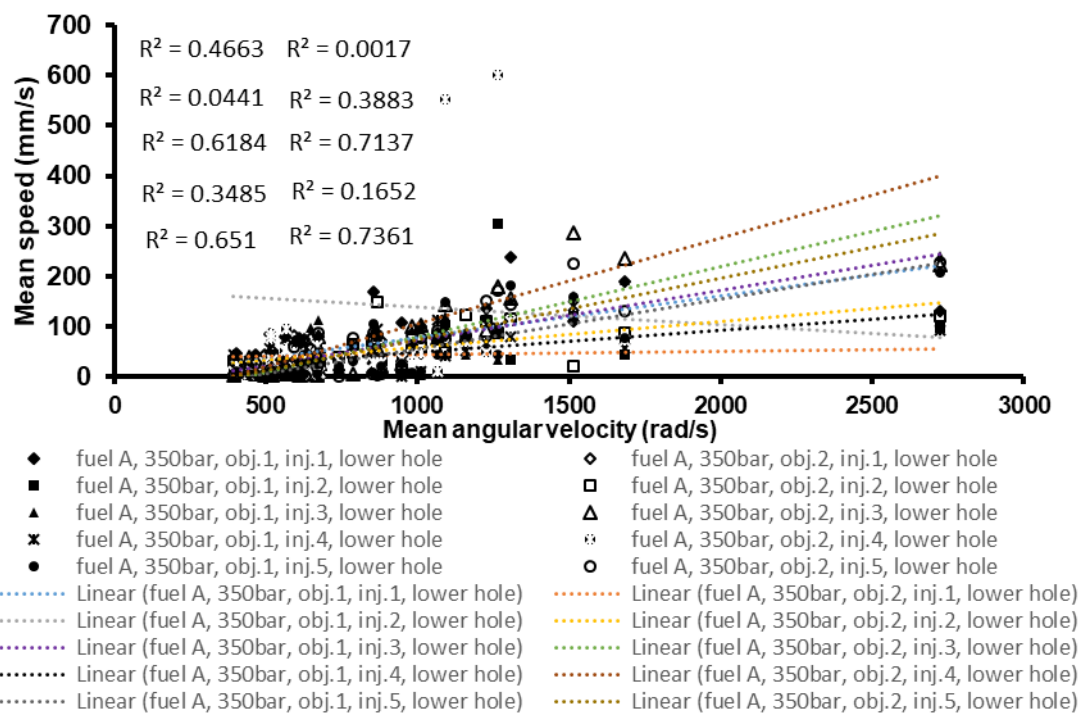
Figure 16: Examples of bubble speeds obtained in nozzle holes, plotted against the corresponding angular velocity of the diesel remaining in the mini-sac following end-of-injection. Linear plots show best linear fits to correlated velocity data and corresponding correlation coefficients.

The fluid/bubble movement in the nozzle holes following injection were unpredictable from injection to injection; i.e. in some cases the fluid/bubbles in both holes were observed to travel outwards, in other cases the fluid travel was inwards (Figure 15); alternatively the fluids were observed to travel in opposite directions to each other. This leads to the conclusion that there were some relatively higher

and lower pressures forming in the mini-sac which led to momentum changes and thus to changes in in-nozzle hole fluid motion and direction of travel.

In order to assess the effect of manufacturing variations on nozzle flow, three acrylic mini-sac nozzles manufactured to the same design (Figure 4 (a)) were employed to investigate the nozzle flow at 250 bar and 350 bar accumulator pressure respectively. The three nozzles tested were designated nozzles A, B and C. The results obtained from the optical observation of the bubble movement inside the upper and the lower holes for 3 acrylic nozzle tips over a set of 250 injection events at 350 bar and 150 injection events at 250 bar are summarised in Table 3.

Table 3: Summary of the fluid movement inside the upper and lower nozzle passages for 3 nozzles at 250 bar and 350bar.

Nozzle Type (Number of Injections)	Nozzle passage (rail pressure (bar))	No. of inward movements	No. of outward movements	No movement
Nozzle A (50)	Upper (250)	0	50	0
Nozzle A (50)	Lower (250)	34	9	7
Nozzle A (50)	Upper (350)	0	50	0
Nozzle A (50)	Lower (350)	31	6	13
Nozzle B (100)	Upper (250)	51	24	25
Nozzle B (100)	Lower (250)	88	0	12
Nozzle B (100)	Upper (350)	35	35	30
Nozzle B (100)	Lower (350)	77	1	22
Nozzle C (100)	Upper (350)	62	15	23
Nozzle C (100)	Lower (350)	17	46	37

Overall (150)	Upper (250)	51	74	25
Overall (150)	Lower (250)	122	9	19
Overall (250)	Upper (350)	97	100	53
Overall (250)	Lower (350)	125	53	72

The measurements reported in Table 3 suggest that the 3 nozzles with the same internal design have produced different post-injection flow behaviour. The flow occurring in the upper hole of Nozzle A was observed to be outward towards the hole exit in all 50 injections examined. On the other hand, the flow occurring in the lower nozzle hole was observed to be inward for 60% - 70% of injections, outward for approximately 15% of injections, and indeterminable or stationary for the remaining 20% of injections. The post-injection flow in the upper hole of nozzle B was observed to be inwards towards the mini-sac for between 35% and 50% of injections, outwards towards the nozzle exit for between 24% and 35% of injections, and indeterminable or stationary for between 25% and 30% of injections. The post-injection flow in the lower hole of nozzle B was observed to be inwards towards the mini-sac for between 77% and 88% of injections, outwards towards the nozzle exit for approximately 1% of injections, and indeterminable or stationary for between 11% and 22% of injections. The post-injection flow in the upper hole of nozzle C was observed to be inwards towards the mini-sac for approximately 62% of injections, outwards towards the nozzle exit for approximately 15% of injections, and indeterminable or stationary for approximately 23% of injections. The post-injection flow in the lower hole of nozzle C was observed to be inwards towards the mini-sac for approximately 17% of injections, outwards towards the nozzle exit for approximately 46% of injections, and indeterminable or stationary for approximately 37% of injections.

The statistics applying to all 3 nozzles show that the flow in the upper hole of all nozzles is inwards towards the mini-sac for approximately 37% of injections, outwards towards the nozzle exit for

approximately 45% of injections, and indeterminable or stationary for approximately 18% of injections. On the other hand, the flow in the lower hole of all nozzles is inwards towards the mini-sac for approximately 62% of injections, outwards towards the nozzle exit for approximately 16% of injections, and indeterminable or stationary for approximately 22% of injections.

The measurements reported in Table 3 reveal that post-injection nozzle hole flows that were inwards towards the mini-sac were common for both upper and lower nozzle holes. These inward flows were significant in that they permitted the admission of external air to the interior of the nozzle holes. If these occurred in a firing diesel engine, they would have permitted the admission of high temperature, high pressure combustion gases to the interior of the nozzle holes.

Figures 17 and 18 are graphs that show the displacement of the vapour structures forming in the nozzle holes between 0.1 ms and 5.5 ms after the end-of-injection (needle re-seal), plotted as a function of frame interval (0.1 ms), for a subset of 10 injections out of 20 subjected to analysis. These correspond to the distance and direction of travel of the vapour structures following the end-of-injection. The black markers and grey markers correspond to vapour structures obtained at 250 bar and 350 bar respectively; each plot type denotes the displacement of a vapour/gas bubble/capsule present in the lower nozzle hole following end-of-injection (specifying the motion of the adjacent liquid) as a function of the frame interval (0.1 ms).

The image analysis methodology adopted here permitted the detection of one or two vapour/gas bubbles/capsules per nozzle hole per injection. These image objects identified represent either two individual bubbles/capsules, or the front and rear interfaces of a large vapour structure. A similar trajectory followed by two objects within the same time period indicates that the two objects correspond to the interfaces of a large vapour capsule. On the other hand, when two image objects are moving independently of each other, it means that these objects correspond to two individual bubbles.
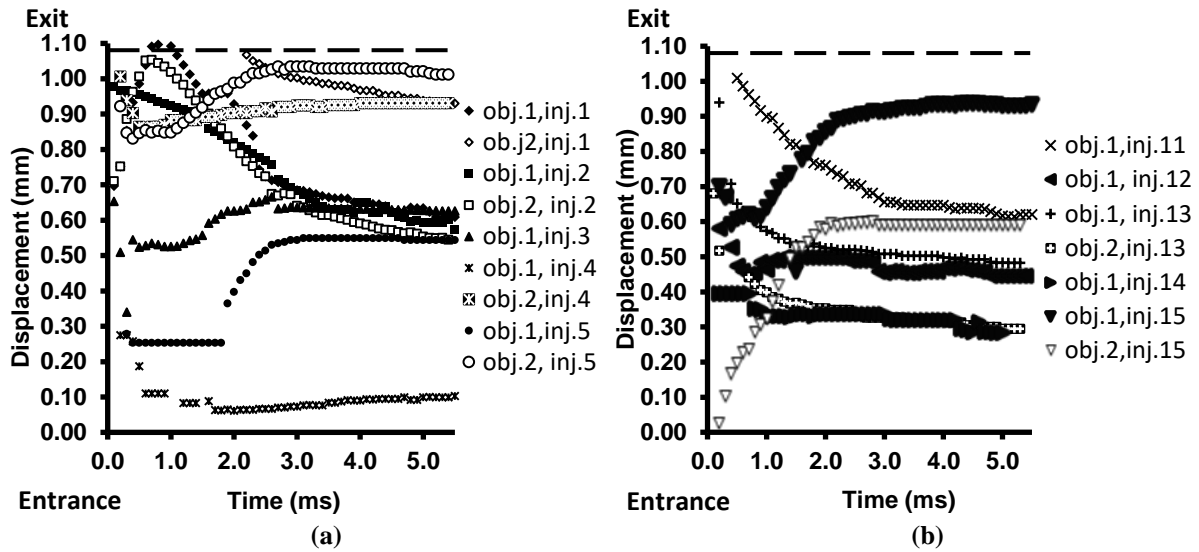
Figure 17: Bubble displacement vs. time graphs for 10 injections ((a) inj.1-5 and (b) 11-15) at 250 bar (lower nozzle hole).
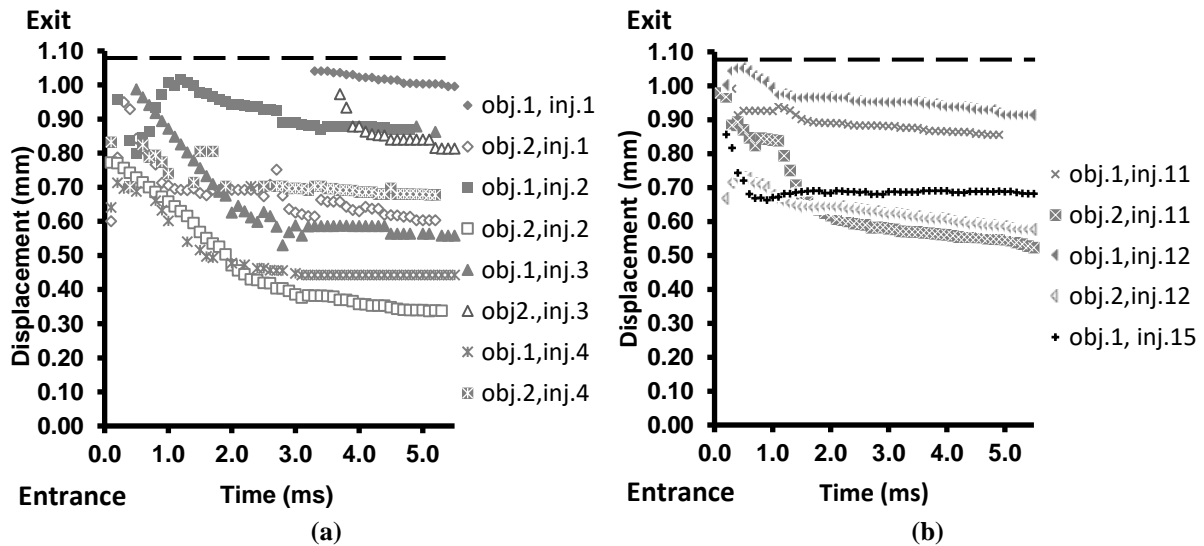

Figure 18: Bubble displacement vs. time graph for 10 injections ((a) inj.1-5 and (b) 11-15) at 350 bar (lower nozzle hole).

The inward movement of vapour structures towards the mini-sac shown in Figures 17 and 18 is represented by a negative slope, while the outward movement of vapour structures towards the nozzle hole exit is represented by a positive slope. The time interval between the measurements is 10^{-4} s (0.1 ms). The mini-sac entrance to the nozzle holes was treated as the origin for the displacement measurements, and the nozzle hole lengths were approximately 1.08 mm (Figure 4 (a)). The location of the nozzle hole exit is denoted by a dashed line in all cases.

The importance in examining the fluid/bubble movement in the nozzle holes following the end-of-injection lies in: (1) any inward movement of the in-nozzle fuel towards the mini-sac permits the admission of external gases into the nozzle holes, and (2) the vapour/gas bubbles and/or capsules forming in the nozzle holes and the mini-sac are believed to contain undissolved oxygen, thereby making the liquid/bubble interface a site of oxidation and oxygen enhanced pyrolysis. For engine operating conditions, the in-cylinder pressure and combustion gas motion during and following combustion increases the probability of external combustion gases gaining access to the nozzle holes and mini-sac.

For example, the first image frame in Figure 12 shows a vapour structure which occupied the entire length of the upper nozzle passage. The regions of high scattering intensity correspond to the capsule/liquid interface, and it is believed that the capsule was surrounded by a thin layer of liquid fuel. Therefore, in the conditions occurring inside an operating diesel engine, this type of gas/vapour structure is able to support oxygen enhanced pyrolysis, which may eventually lead to deposit formation at various locations in the injector nozzles (nozzle hole entrances, nozzle hole passage interior surfaces, and in the mini-sac).

Figure 19 is a sequence of 6 image frames obtained at 0.5 ms intervals, which show how the diesel fuel and vapour in the lower hole were drawn towards the mini-sac following the end-of-injection, permitting external air admission to the nozzle hole (the red curve in the bottom nozzle hole). In this sequence of image frames, a vapour capsule was sucked back into the mini-sac, followed by a short column of liquid, with a liquid-gas interface which retreated towards the mini-sac before stopping two-thirds the way down the hole. The gas at the interface of the retreating liquid was just the surrounding air gaining admittance to the nozzle hole.
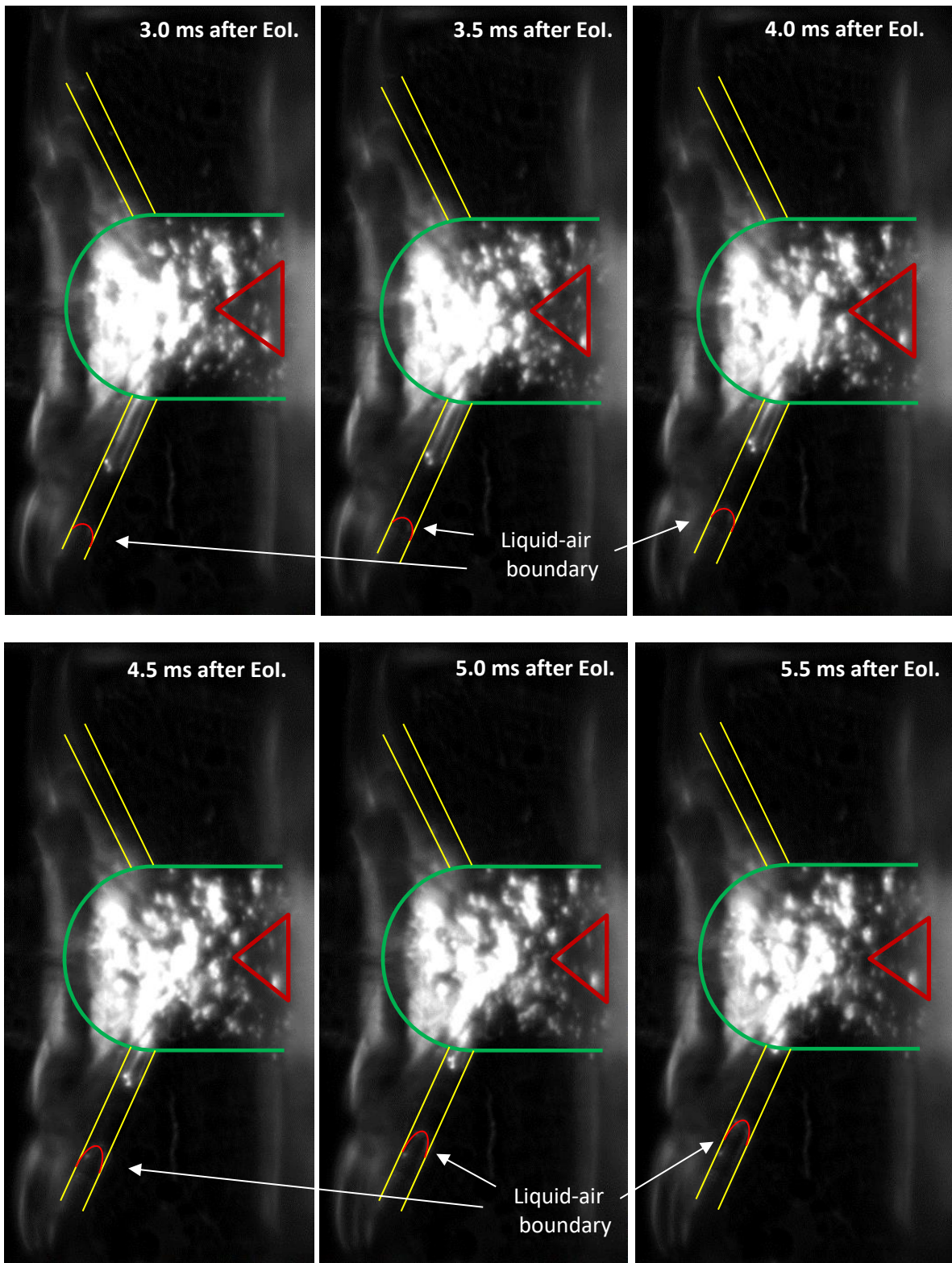
Figure 19: A Sequence of 6 image frames at 1.0 ms intervals, showing the inward flow of a vapour capsule and a diesel liquid column in the lower nozzle hole following EoI, followed by admission of external air into the lower nozzle hole (Nozzle A).

Figure 20 is a sequence of 6 image frames. The first image frame was obtained at 0.1 ms after end-of-injection. The second to sixth image frames were obtained at 0.2 ms intervals, from 0.5 ms to 1.3 ms after end-of-injection. This sequence of image frames shows the post-injection formation of a gas/vapour capsule in the upper nozzle hole that extends all the way from the upper nozzle hole exit to the mini-sac. For a brief period, external air was able to gain access to the mini-sac directly, before the circumferential motion of the liquid diesel in the mini-sac pushed a column of liquid into the nozzle hole, causing the air column to retreat up the hole towards the hole exit. The external air column and the liquid were then observed to reach mechanical equilibrium with the phase interface located half way down the nozzle hole.
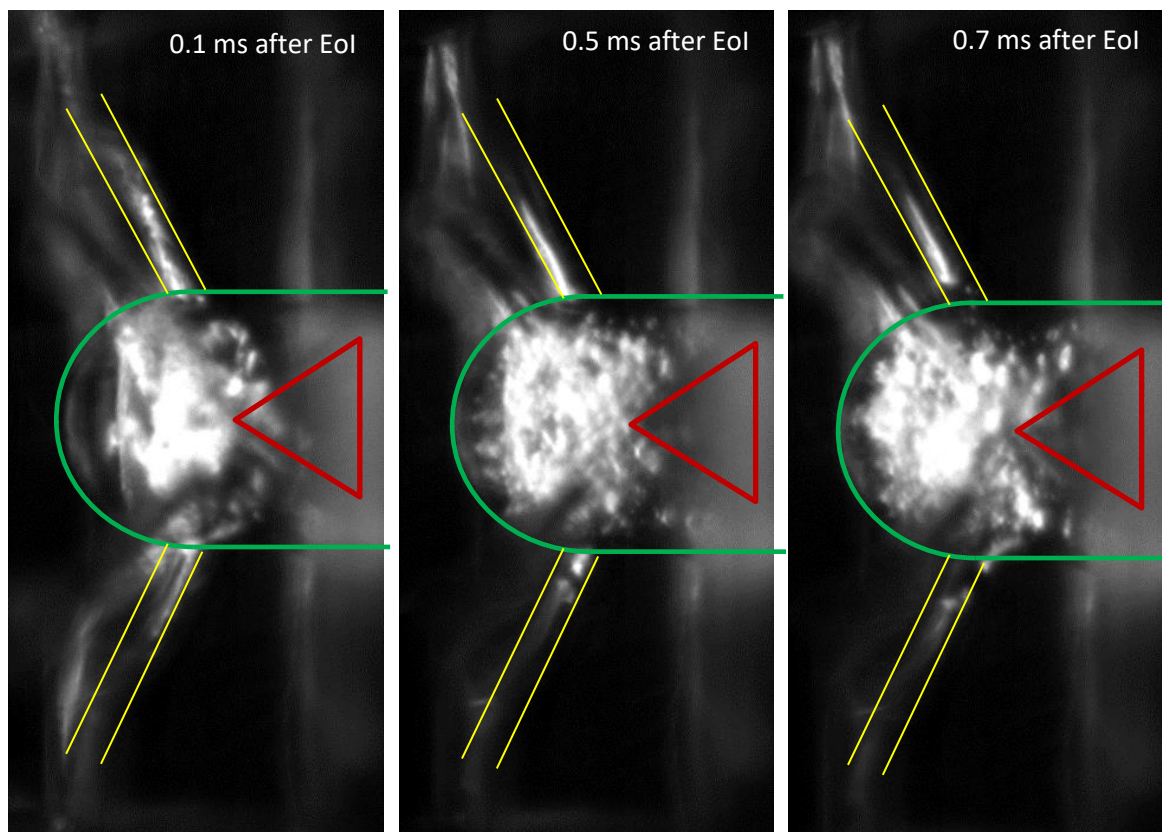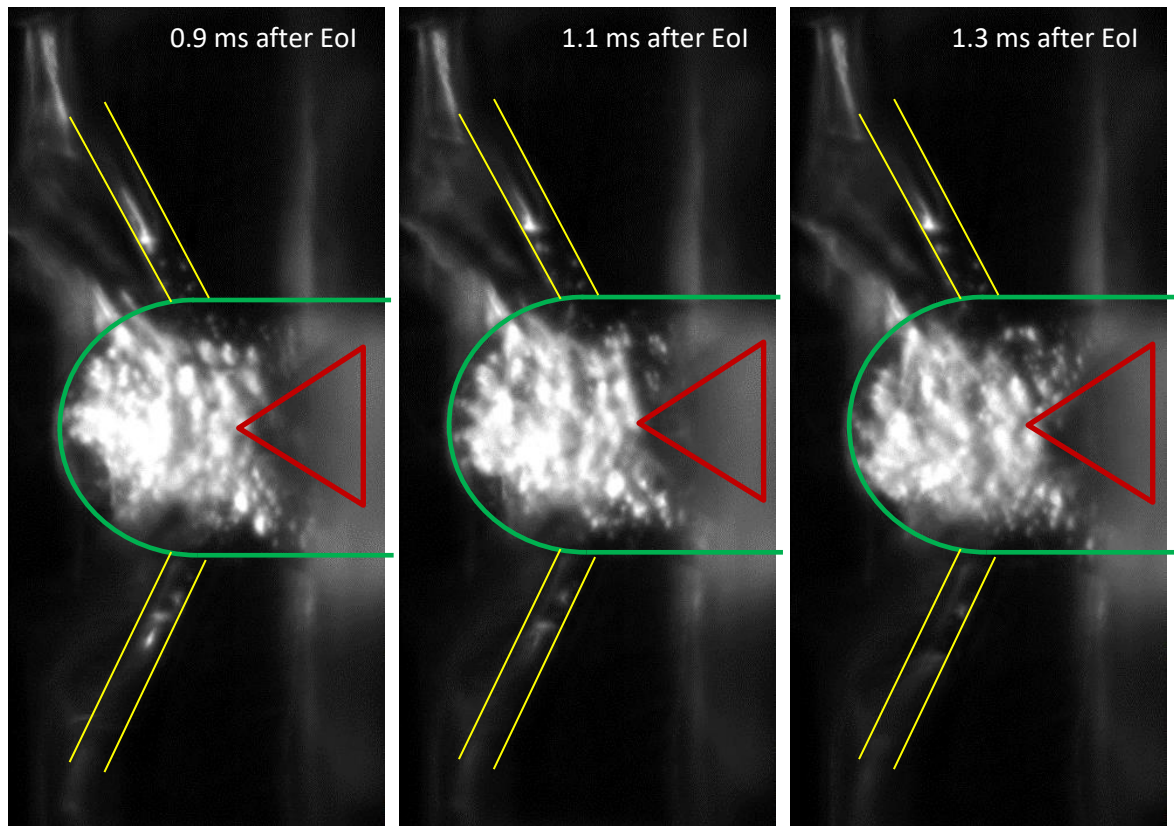
Figure 20: A sequence of image frames obtained at 0.2 ms intervals, showing external air gaining access to the diesel liquid in the mini-sac via the upper nozzle hole following EoI. At 0.5 ms after EoI, the flow in the mini-sac began to pump liquid into the upper hole, pushing the air-liquid interface down the hole (Nozzle C).

The sequence of image frames shown in Figures 19 and 20 reveal how external air was able to gain access to the nozzle holes during the post injection period between successive injections. In a firing diesel engine, the post-injection combustion gas would be admitted to the nozzle hole at high pressure and temperature, comprised of O_2, N_2, H_2O, CO, CO_2 and unreacted hydrocarbons. These gaseous components would encounter a liquid diesel fuel film on the interior walls of the nozzle holes, and the liquid diesel at the phase interface. The interface between hot combustion gases and liquid diesel will support local oxidation and oxidation enhanced pyrolysis, potentially leading to layered deposition.

4.5 Analysis of Buoyancy Effects

The horizontal orientation of the injector and the biased measurements of the bubble/capsule movement inside the nozzle passages (Table 3) raise the question as to whether the induced nozzle flow was a result of buoyancy effects, or of the pressure differences induced by the motion of the liquid fuel inside the mini-sac following the end-of-injection. This consideration led to an analysis of the terminal

velocity achieved by the vapour/gas bubbles/capsules in the nozzle holes, if the motion was induced by buoyancy forces. These were to be compared with the nozzle flow velocities actually observed. According to Plesset and Epstein [40], bubble motion of an air/diesel vapour bubble due to buoyancy in diesel fuel is determined using Equations 8 and 9. The range of bubble sizes chosen for this analysis corresponded to the range of bubble sizes measured in the nozzle hole passages. Equation 9 is Rybczynski's formula [41], which takes into account both buoyancy and drag forces.

$$F_R = \left(^{4\pi}/_3\right)g(\rho_L - \rho_G)R^3 \tag{8}$$

$$F_R = 6\pi\mu_L Ru\frac{2\mu_L+2\mu_G}{3\mu_L+3\mu_G} => u = \frac{F_R(3\mu_L+3\mu_G)}{6\pi\mu_L R(2\mu_L+2\mu_G)} \tag{9}$$

where μ_L is the liquid viscosity, μ_G the vapour/gas viscosity, ρ_L the liquid density (kg/m^3), ρ_G the gas density (kg/m^3), R the bubble radius (m), u the terminal velocity (m/s), F_R the buoyancy force (N), and g the gravitational acceleration (m/s^2).

On the other hand, the actual velocity of the vapour structures inside the passages was determined using the results of the nozzle flow analysis. In particular, the bubble velocities were equal to the bubble displacement per unit time. This is expressed mathematically in Equation (10).

$$u_{actual} = \frac{\Delta l}{\Delta t} \tag{10}$$

where u_{actual} is the actual bubble velocity (mm/s), Δl the bubble displacement (mm), and Δt the time interval between image frames (s).

Figure 21 shows that the mean terminal velocity of the bubbles due to buoyancy (black square marker) was one to two orders of magnitude smaller than the mean actual bubble velocities (black dots and crosses) calculated directly from the experimental data. This comparison suggests that the bubble motion inside the nozzle passages was not a consequence of buoyancy, but by the pressure gradients

generated by the post-injection rotational motion of the fuel in the mini-sac, relative to the ambient air surrounding the injector.
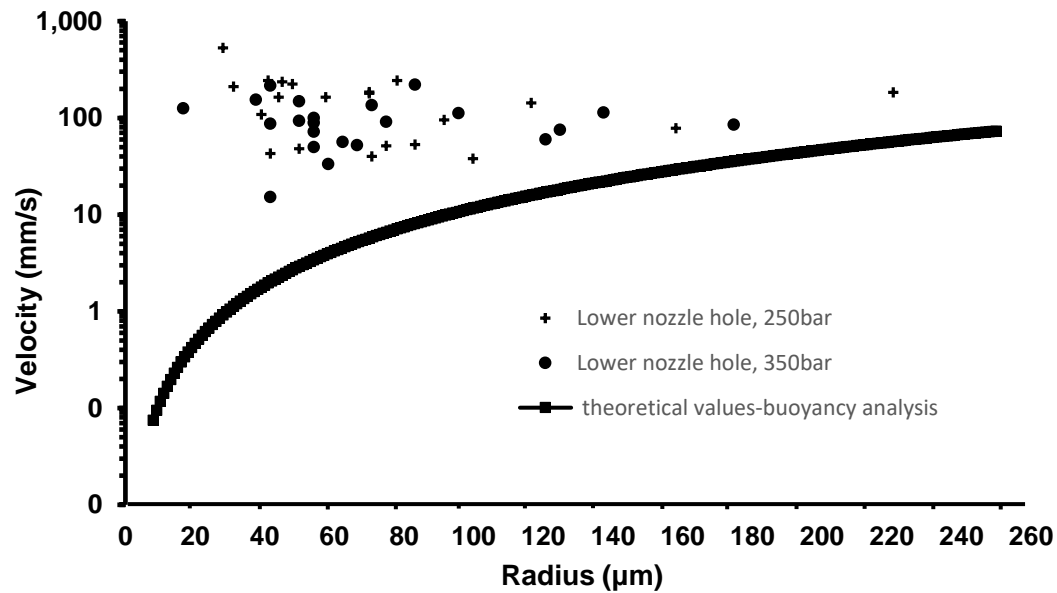

Figure 21: Experimental bubble velocity inside the lower hole and bubble velocity due to buoyancy as a function of bubble size.

4.6 Implications for Internal Nozzle Deposits

4.6.1 Mini-Sac Deposits and Deposit Precursors

The observations and measurements of the post-injection flows occurring in the mini-sac and nozzle holes discussed previously suggest that three distinct processes may be indicated in mini-sac deposition in diesel injectors. The first process that may lead to deposition in the mini-sac arises from the long-term contact between the diesel liquid and the mini-sac steel surface occurring between injections (30 ms between successive injections at high speed, rising to 100 ms between injections at engine idle). The diesel liquid in the mini-sac in contact with the local steel surface attains mechanical equilibrium between successive injections with a temperature in the range of 450 K – 550 K. The surrounding injector nozzle steel temperature may be significantly larger, due to the heat transfer that occurs from the air and combustion gases to the nozzle during air compression, combustion and expansion. The surface of contact between the diesel fuel and the nozzle walls is likely to support accelerated fuel ageing and/or pyrolysis reactions, which can lead to the formation and deposition of lacquers, sticky

components and crusty carbonaceous particulates, which are able to condense, settle and aggregate in surface irregularities and/or internal surface cracks.

The second process that may lead to deposit precursors forming in the mini-sac arises from the formation of the post-injection mini-sac bubble cloud, which, once formed, is able to take up approximately 25% of the mini-sac volume. These bubble clouds are observed to form in the mini-sac following the end-of-injection for every injection, and are comprised of diesel fuel vapour, and undissolved molecular Oxygen and Nitrogen, at temperatures in the range of 450 K – 550 K. The oxygen present in the bubble cloud is likely to initiate oxidation and oxidation enhanced pyrolysis in the liquid film surrounding the bubble cloud. This oxidation process is short-lived (30 ms – 100 ms between successive injections), that is likely to be ended once the next injection occurs. It is thus unlikely that mini-sac bubble cloud-liquid oxidation enhanced pyrolysis is a significant contributor to mini-sac deposition.

The third process that may lead to deposit precursors forming at the entrances to the nozzle holes arises through oxygen containing gas/vapour capsules or external gas/vapour columns (external gas admission to nozzle holes) reacting with liquid diesel fuel films located in the neighbourhood of the nozzle hole entrances. If geometric cavitation (film cavitation) occurs at the inlet of the nozzle holes during fuel injection, then deposit precursors may be able to form and settle in surface irregularities/cracks near the nozzle hole entrances, and continue to grow through reaction-based condensation of oxidation assisted pyrolysis products and/or aggregation (layered lacquers, polymers, insoluble, sticky, oxygenated gums and crusty carbonaceous particulates).

4.6.2 Nozzle Hole Deposits and Deposit Precursors

Previous chemical analyses of nozzle deposits inside diesel injector nozzle holes obtained from engines has demonstrated the presence of elements and compounds that have originated from cylinder liner lubricant oil. This suggests that external combustion gases (which include components present in the engine lubricant oil) have been able to gain access to the interior of the nozzle holes, which are therefore

likely to be involved in the initiation and formation of deposits. However, the physical mechanism responsible for permitting this access has hitherto been unknown.

The observations and measurements of the post-injection flows occurring in the nozzle holes discussed earlier suggest that two distinct processes may be indicated in nozzle hole deposition in diesel injectors. The first process that may lead to deposition in the nozzle holes is the same as the first process discussed in Section 4.5.1 above, and arises from the long-term contact between the diesel liquid and the internal nozzle hole steel surfaces occurring between injections (30 ms period between successive injections at high speed, rising to 100 ms between injections at engine idle). The surface of contact between the diesel fuel and the nozzle hole walls is likely to support accelerated fuel ageing and/or pyrolysis reactions, which can lead to the formation/deposition of lacquers and crusty carbonaceous particulates, which are able to condense, settle and aggregate in surface irregularities and internal surface cracks.

The second process that may lead to deposit precursors forming in the nozzle holes arises through oxygen containing gas/vapour capsules or external gas/vapour columns (external gas admission to nozzle holes) reacting with liquid diesel fuel films located on the internal steel walls of the nozzle holes. The observations and measurements reported in the sections above demonstrate that the post-injection momentum-driven evacuation of fuel liquid from the mini-sac and nozzle holes produces vapour capsules inside the nozzle holes extending all the way along the holes that connect the mini-sac to the external surroundings. This permits external gases to enter the nozzle holes, mix with fuel vapour and form a contact surface with the fuel liquid film remaining attached to the nozzle walls. Furthermore, circumferential motion of the diesel liquid in the mini-sac caused movement of the liquid fuel and vapour bubbles/capsules remaining in the nozzle holes. This motion was inwards towards the mini-sac for some of the nozzle holes, outwards towards the nozzle hole exits for the remainder, and was unpredictable from injection to injection. The measurements reported earlier suggest that the post-injection diesel flow in the mini-sac establishes relative pressure differences across the nozzle holes, which are capable of producing inward flows of fuel towards the mini-sac in some of the holes, and outward flows towards the nozzle exits in the remainder.

The phase boundaries that develop in the nozzle holes during vapour capsule formation following the end-of-injection and during the later inward flows retreat towards the mini-sac, permitting the admission of hot, post-injection combustion gases. These are comprised of major species O_2, N_2, H_2O, CO, and CO_2, together with small concentrations of unburned hydrocarbons, particulates and oil components. When these combustion gases enter the injector nozzle passages, they will encounter wet surface films of diesel fuel on the walls of the nozzle passages.

During normal engine operation, the temperature of the injector bodies in the cylinders are in the range of 450 K – 600 K. The exhaust gas-liquid film interfacial surfaces found in the nozzle hole passages during and following combustion are likely to be regions of polymerization, non-premixed oxidation, and oxygen activated pyrolysis reactions. The composition of crude-oil derived diesel is approximately 70 % paraffins, 25 % mono-aromatics, 3 % di-aromatics, and 1 % tri-aromatics [42]. Non-premixed oxidation, oxygen activated pyrolysis, conventional thermal pyrolysis and polymerization results in various products and particulate formation, that is likely to settle on the walls of the injector passages. These layers are able to grow and harden through condensation, adsorption, reaction, aggregation, and thermal tempering, leading to the formation of hard lacquers, polymer layers, oxygenated gums, and crusty, carbonaceous deposits [26].

5. Conclusions

An optical method has been developed and utilized for time-resolved imaging and measurement of the internal diesel nozzle flow, in order to investigate the relationship between the post-injection flow occurring in the nozzle mini-sac and the nozzle flow occurring inside the upper and lower nozzle passages, as a function of rail pressure. The experimental configuration was based on high-speed, high resolution imaging of elastic scattering produced by white light incident on the liquid-vapour interfaces of the structures formed after the end-of-injection. The time-resolved scattering data were employed to produce bubble size and pressure difference distributions, together with graphs showing the correlated motion of the fluid/bubbles in the passages with the rotational motion of the fluid in the mini-sac.

The analysis of the experimental data has led to the following conclusions:

1. A large vapour/bubble cloud and vapour bubbles/capsules were observed to form in the mini-sac and nozzle holes respectively following the end-of-injection. These formations occurred as a result of momentum-driven evacuation of diesel liquid in the mini-sac and nozzle holes following needle closure at the end-of-injection. This caused the local fluid pressure to drop below the saturated vapour pressure of diesel, permitting phase transition.

2. Vapour capsules that formed in the nozzle holes following the end-of-injection were observed to extend the full length of the nozzle holes connecting the mini-sac to the external surroundings. This permitted external gases to gain entry to and mix with the diesel vapour filling the nozzle holes, and to form a contact layer with the liquid fuel film remaining attached to the nozzle hole walls.

3. Bubbles formed in the mini-sac following the end-of-injection were observed to collectively rotate in the mini-sac, reflecting the circumferential motion of the remaining diesel liquid. An increase in rail pressure led to larger initial angular velocity of the post-injection mini-sac circumferential flow; however, the decay rate of the circumferential flow appeared to be independent of the rail pressure, and is expected to be determined by the viscosity of the diesel.

4. The bubble sizes formed inside the nozzle mini-sac appeared to remain unchanged throughout the post-injection period, including during the relaxation of the flow. These bubbles produced pressure difference distributions that suggested that they were comprised of a mixture of diesel vapours and undissolved gas. It is likely that the undissolved gas was comprised of oxygen and nitrogen that evaporated out of solution during low pressure rarefraction that occurred after the pressure wave passed through the nozzle mini-sac and holes following the end-of-injection. These multi-component gas/vapour bubbles are able to initiate oxidation and pyrolysis reactions when operating in diesel engine

conditions, which may lead to deposit precursor formation in the mini-sac, and on the lower needle surface.

5. Vapour bubbles/capsules were observed to be formed in the nozzle hole passages following the end-of-injection. These were observed to move in concert with the surrounding diesel liquid. The diesel nozzle flow induced in the nozzle passages following the end-of-injection was found to be correlated with the post-injection rotational flow that developed inside the nozzle mini-sac, and could not be a consequence of buoyancy. The post-injection nozzle flows were observed to relax in concert with the decay of the circumferential flow occurring in the mini-sac. It is expected that the rate of change of angular velocity is determined by the viscosity of the diesel.

6. The vapour structures forming in the nozzle hole passages were observed to move inwards towards the mini-sac for a substantial fraction of injections, and either outwards towards the nozzle exit or remain stationary for the remainder of the injections. The post-injection inwards motion of the liquid fuel remaining in the nozzle holes towards the mini-sac leaves a wet film of diesel liquid coating the walls of the nozzle passages, and permit the admission of external gas into the nozzle hole passages.

In an operating diesel engine, this process would permit the admission of high temperature combustion gases (containing O_2, N_2, H_2O, CO_2, and CO as main species) from the combustion chamber into the nozzle holes. These gases are able to react with the liquid diesel films coating the walls of the nozzle passages and the retreating liquid surfaces to form surface deposits and/or deposit precursors.

References

1. Stumpp, G. and Ricco, M., "Common Rail - An Attractive Fuel Injection System for Passenger Car DI Diesel Engines", SAE Technical Paper 960870 (1996). https://doi.org/10.4271/960870.

2. Guerrassi, N. and Dupraz, P., "A Common Rail Injection System For High Speed Direct Injection Diesel Engines", SAE Technical Paper 980803 (1998). https://doi.org/10.4271/980803.

3. Oki, M., Matsumoto, S., Toyoshima, Y., Ishisaka, K. et al., "180MPa Piezo Common Rail System", SAE Technical Paper 2006-01-0274 (2006). https://doi.org/10.4271/2006-01-0274.

4. Fettes, C. and Leipertz, A., "Potentials of a Piezo-Driven Passenger Car Common Rail System to Meet Future Emission Legislations - An Evaluation by Means of In-Cylinder Analysis of Injection and Combustion", SAE Technical Paper 2001-01-3499 (2001). https://doi.org/10.4271/2001-01-3499.

5. H. Kyu, S. Sung Wook Park, C. Sik Leea, "Effect of piezo-driven injection system on the macroscopic and microscopic atomization characteristics of diesel fuel spray", *Fuel* Vol. 86: 17 – 18 (2007) 2833 – 2845. https://doi.org/10.1016/j.fuel.2007.03.015.

6. Bianchi, G., Pelloni, P., Filicori, F., and Vannini, G., "Optimization of the Solenoid Valve Behavior in Common-Rail Injection Systems", SAE Technical Paper 2000-01-2042 (2000). https://doi.org/10.4271/2000-01-2042.

7. Boehner, W. and Hummel, K., "Common Rail Injection System for Commercial Diesel Vehicles", SAE Technical Paper 970345 (1997). https://doi.org/10.4271/970345.

8. Bae, C., Yu, J., Kang, J., Kong, J. et al., "Effect of Nozzle Geometry on the Common-Rail Diesel Spray", SAE Technical Paper 2002-01-1625 (2002). https://doi.org/10.4271/2002-01-1625.

9. Han, J., Lu, P., Xie, X., Lai, M. et al., "Investigation of Diesel Spray Primary Break-up and Development for Different Nozzle Geometries", SAE Technical Paper 2002-01-2775 (2002). https://doi.org/10.4271/2002-01-2775.

10. Mahr B., "Future and Potential of Diesel Injection Systems". In: Whitelaw J.H., Payri F., Arcoumanis C., Desantes J.M. (eds) *Thermo- and Fluid Dynamic Processes in Diesel Engines 2*. Springer, Berlin, Heidelberg.(2004). https://doi.org/10.1007/978-3-662-10502-3_1

11. Shinohara Y, Takeuchi K., Herrmann O., Laumen H., "Mixture Formation – 3000 Bar Common Rail System", *54417963-MTZ-Worldwide* Vol. 72(1) (2011) 4 – 9, Springer Shinohara.

12. Graham M., Keeler N. and Kewley J., "Ultra-high Pressure Common Rail Systems", *Injection Systems for IC Engines*, IMechE, London, 13 – 14 May 2009, pp. 231 – 243, Chandos Publishing, ISBN 9781843345619.

13. Caprotti R., Breakspear A., Graupner O., Klaua T., "Detergency Requirements of Future Diesel Injection Systems", SAE Technical Paper 2005-01-3901 (2005). https://doi.org/10.4271/2005-01-3901.

14. Caprotti R., Breakspear A., Graupner O., Klaua T., Kohnen O., "Diesel Injector Deposits Potential in Future Fuelling Systems", SAE Technical Paper 2006-01-3359 (2006). https://doi.org/10.4271/2006-01-3359

15. Tang J., Pischinger S., Lamping M., Korfer T., Tatur M., Tomazic D., "Coking Phenomena in Nozzle Orifices of DI-Diesel Engines", *SAE International Journal of Fuels and Lubricants* Vol. 2:1 (2009) pp. 259 – 272.

16. Barker J., Richard P., Snape C., and Meredith W., "Diesel Injector Deposits - An Issue That Has Evolved with Engine Technology", SAE Technical Paper 2011-01-1923 (2011). https://doi.org/10.4271/2011-01-1923.

17. Payri F., Bermudez V., Payri R., Salvador F., "The influence of cavitation on the internal flow and the spray characteristics in diesel injection nozzles", *Fuel* Vol. 84: 4 – 5 (2004) 419 – 431. https://doi.org/10.1016/j.fuel.2003.09.010.

18. Andriotis A., Gavaises M., Arcoumanis C., "Vortex flow and cavitation in diesel injector nozzles", *Journal of Fluid Mechanics* Vol. 610 (2008) 195 – 215. https://doi.org/10.1017/S0022112008002668.

19. Ullmann J., Geduldig M., Stutzenberger H., Caprotti R., Balfour G., "Investigation into the Formation and Prevention of Internal Diesel Injector Deposits". SAE Technical Paper 2008-01-0926 (2008). https://doi.org/10.4271/2008-01-0926.

20. Birgel A., Ladommatos N., Aleiferis P., Zulch S., Milovanovic N., Lafon V., Orlovic A., Lacey P., Richards P., "Deposit Formation in the Holes of Diesel Injector Nozzles: A Critical Review", SAE Technical Paper 2008-01-2382 (2008). https://doi.org/10.4271/2008-01-2383.

21. Schwab S., Bennett J., Dell S., Galante-Fox J., Kulinowski A., Miller K. "Internal Injector deposits in high-pressure common rail diesel engines", SAE Technical Paper 2010-01-2242 (2010). https://doi.org/10.4271/2010-01-2242.

22. Barker J., John Langley G., Richards P., *"Insights into Deposit Formation in High Pressure Diesel Fuel Injection Equipment"*, SAE Technical Paper 2010-01-2243 (2010). https://doi.org/10.4271/2010-01-2243

23. Ikemoto M., Omae K., Nakai K., Ueda R., Kakekashi N., Sunami K., *"Injection Nozzle Coking Mechanism in Common-rail Diesel Engine"*, SAE Technical Paper 2011-01-1818 (2011). https://doi.org/10.4271/2011-01-1818.

24. Birgel A., Ladommatos N., Aleiferis P., Milovanovic N., Lacey P. and Richards P., "Investigations on Deposit Formation in the Holes of Diesel Injector Nozzles", *SAE International Journal of Fuels and Lubricants* Vol. 5:1 (2012) pp. 123-131. https://doi.org/10.4271/2011-01-1924.

25. Lacey P., Gail S., Kientz J., Benoist G., Downes P., Daveau C., "Fuel Quality and Diesel Injector Deposits", SAE Technical Paper 2012-01-1693 (2012). https://doi.org/10.4271/2012-01-1693.

26. Barker J., Snape C., Scurr D., "Information on the Aromatic Structure of Internal Diesel Injector Deposits from Time of Flight Secondary Ion Mass Spectrometry", SAE Technical Paper 2014-01-1387 (2014). https://doi.org/10.4271/2014-01-1387.

27. Smith A., Williams R., "Linking the physical manifestation and performance effects of injector nozzle deposits in modern diesel engines", *SAE International Journal of Fuels and Lubricants* Vol. 8:2 (2015) pp. 344 – 357. https://doi.org/10.4271/2015-01-0892.

28. Rounthwaite, N., Williams, R., McGivery, C., Jiang, J. et al., "A Chemical and Morphological Study of Diesel Injector Nozzle Deposits - Insights into their Formation and Growth Mechanisms", *SAE International Journal of Fuels and Lubricants* Vol. 10:1 (2017) Paper 2017-01-0798. https://doi.org/10.4271/2017-01-0798.

29. d'Ambrosio S., Ferrari A., "Diesel Injector Coking: Optical-Chemical Analysis of Deposits and Influence on Injected Flow Rate, Fuel Spray and Engine Performance", *Transactions of the ASME: Journal of Engineering for Gas Turbines and Power* Vol. 134 (2012) 062801-1 – 062801-14. https://doi.org/10.1115/1.4005991.

30. Fatmi, Z, "Optical and Chemical Characterization of the Effects of High-pressure Hydrodynamic cavitation on Diesel Fuel", PhD Thesis, City, University of London (2019).

31. Lockett R., Jeshani M., "An experimental investigation into the effect of hydrodynamic cavitation on diesel", *International Journal of Engine Research* Vol. 14:6 (2013) pp. 606 – 621. https://doi.org/10.1177/1468087413497005.

32. Jeshani M., "Optical Characterization of Cavitating Flows in Diesel Fuel Injection Equipment", PhD Thesis, City, University of London (2014).

33. Lockett, R., Fatmi, Z., Kuti, O. and Price, R., "An Investigation into the Effect of Hydrodynamic Cavitation on Diesel using Optical Extinction", *Journal of Physics: Conference Series* Vol. 656:1 (2015) Paper 012091. https://doi.org/10.1088/1742-6596/656/1/012091.

34. Price R., Blazina D., Smith C., Davies T., "Understanding the impact of cavitation on hydrocarbons in the middle distillate range", *Fuel* Vol. 156 (2015) pp. 30 – 39. https://doi.org/10.1016/j.fuel.2015.04.026.

35. Lockett, R., Fatmi, Z., Kuti, O., and Price, R., "An Optical Characterization of the Effect of High-Pressure Hydrodynamic Cavitation on Diesel", SAE Technical Paper 2016-01-0841 (2016). https://doi.org/10.4271/2016-01-0841.

36. K. Makri, "The Characterization of Internal Diesel Flow and External Spray Structure using Laser Diagnostics", PhD Thesis, City, University of London (2018).

37. Lockett R., Liverani L., Thaker D., Jeshani M, Tait N., "The characterisation of diesel nozzle flow using high speed imaging of elastic light scattering", *Fuel* Vol. 106 (2013) 605 – 616. https://doi.org/10.1016/j.fuel.2012.10.065.

38. Mylapilli L., Gogula P., Arya A., "Hydraulic and Surge Analysis in a Pipeline Network using Pipeline Studio", *International Journal of Engineering Research and Technology* Vol 4:2(2015) 41-48.

39. National Cooperative Refinery Association (NCRA). Material Safety Data Sheet, http://www.petrolab.com: (2016).

40. Epstein P., Plesset M., "On the stability of gas bubbles in liquid-gas solutions", *Journal of Chemical Physics* Vol. 18:11 (1950) pp. 1505 – 1509. [39] Lamb H. *Hydrodynamics*. 6th ed. London: Cambridge University Press; 1932.

41. Lamb H. *Hydrodynamics*. 6th ed. London: Cambridge University Press; 1932.

42. Erwin J. "Assay of diesel fuel components properties and performance". In: *Symposium on processing and product selectivity of synthetic fuels*, Division of Fuel Chemistry, American Chemical Society, Washington, USA, 23–28 August 1992, 1915 – 1923.